

FLORIDA STATE UNIVERSITY
COLLEGE OF ARTS AND SCIENCES

TOWARD DATA-DRIVEN SUBGRID-SCALE MODELING OF THE ZEL'DOVICH
DEFLAGRATION-TO-DETONATION MECHANISM IN DENSE STELLAR PLASMAS

By

BRANDON L. GUSTO

A Dissertation submitted to the
Department of Scientific Computing
in partial fulfillment of the
requirements for the degree of
Doctor of Philosophy

2023

Copyright © 2023 Brandon L. Gusto. All Rights Reserved.

arXiv:2401.16674v1 [astro-ph.SR] 30 Jan 2024

Brandon L. Gusto defended this dissertation on April 3rd, 2023.

The members of the supervisory committee were:

Tomasz Plewa
Professor Directing Traffic

Mark Sussman
University Representative

Adrian Barbu
Committee Member

Bryan Quaipe
Committee Member

Olmo Zavala
Committee Member

The Graduate School has verified and approved the above-named committee members, and certifies that the dissertation has been approved in accordance with university requirements.

This dissertation is dedicated to my loving family: to my mother and father, Renee and Jeffrey, my older brother, Cody, and my little sister, Jenna. Also to my wonderful fiancé, Marie. Finally, of course to my Oma who never expected anything less than a doctorate degree. Without their love and support this manuscript would not have been possible.

ACKNOWLEDGMENTS

The author would like to first acknowledge the Science, Mathematics, and Research for Transformation (SMART) Scholarship-for-Service Program for providing support for this work. Additionally, he would like to thank his advisor, Dr. Tomasz Plewa for his unwavering support and guidance; Tomasz's dedication to his students and his passion for scientific truth has been a constant source of inspiration. The author also would like to thank Dr. Christoph Federrath from the Australian National University for his help in establishing turbulence driving parameters over many constructive virtual meetings.

TABLE OF CONTENTS

List of Tables	vii
List of Figures	viii
List of Symbols	xii
Abstract	xiii
1 Introduction	1
1.1 Motivation and outline	1
1.2 Relevant combustion physics	1
1.2.1 Spontaneous detonation	2
1.2.2 Flame acceleration	4
1.3 Thermonuclear supernova explosion scenario	5
2 Challenges of Modeling Thermonuclear Supernovae	9
2.1 Introduction	9
2.2 Modeling of DDT	11
2.2.1 Conditions for the transition to detonation	11
2.2.2 Turbulent conditions in the deflagrating white dwarf	13
2.2.3 Modeling domains	14
2.3 Computational modeling	15
2.3.1 Finite volume discretization	16
2.3.2 Multiresolution based adaptive mesh refinement	16
2.3.3 Additional remarks	17
3 Direct Numerical Simulation of the Deflagration-To-Detonation Transition	19
3.1 Introduction	19
3.2 Methods	19
3.2.1 Idealized initial conditions	20
3.2.2 Realistic initial conditions	22
3.2.3 Analysis approach	24
3.3 Results	24
3.3.1 Idealized initial conditions	26

3.3.2	Realistic initial conditions	32
3.4	Discussion	35
3.4.1	A critical radius for detonation	36
3.4.2	Concluding remarks	37
4	A Data-Driven Model for DDT	38
4.1	Introduction	38
4.2	Methods	38
4.2.1	Feature selection	40
4.2.2	Neural network architecture	43
4.2.3	Performance metrics	45
4.2.4	Using the classifier as a subgrid-scale model	46
4.3	Results	47
4.3.1	Naive strategy	47
4.3.2	Khokhlov strategy	49
4.3.3	Performance summary	50
4.3.4	Verification of the subgrid-scale model in the <i>a posteriori</i> setting	53
4.4	Discussion	56
4.4.1	On the use of the classifier as a subgrid-scale model	58
4.4.2	Notes on convergence of network accuracy	58
5	Summary	60
	Appendix	
A	Analysis of Turbulent Perturbations	62
B	Data Preparation, Data Augmentation, and Hyperparameter Tuning	65
B.1	Data preparation	65
B.2	Data augmentation	65
B.3	Hyperparameter tuning	66
C	Neural Network Model Evaluation in Proteus	67
	Bibliography	69
	Biographical Sketch	74

LIST OF TABLES

3.1	Description of databases showing the range of ambient density and temperature for each database as well as the normalized amplitude and width (for Gaussian models). The total number of configurations is shown for each database.	25
4.1	Summary of the network architectures resulting from the hyperparameter tuning process. For each of the four models, N1, N2, N3, and N4, the table shows the number of convolutional filters (<code>nfilters</code>), filter size (<code>filtersz</code>), use of pooling (<code>dopool</code>), number of dense layer nodes (<code>nodes</code>), and dropout percentage (<code>dropout</code>). The n th convolutional layer is labeled as <code>clyr_n</code> , and the n th dense layer is labeled as <code>dlyr_n</code>	49
4.2	Summary of results for the methods introduced in Equations (4.2) to (4.6) and Equations (4.7) to (4.8) on the validation samples from datasets <code>td.naive.synthetic</code> , <code>td.naive.turb</code> , <code>td.khokhlov.synthetic</code> , and <code>td.khokhlov.turb</code>	51
B.1	Summary of hyperparameters allowed to change freely, and the range of values that they are allowed to assume in the hyperparameter tuning process.	66

LIST OF FIGURES

1.1	Simulated evolution of peak temperature within the core region of a white dwarf up to the moments of ignition. The inset shows the rapid temperature rise occurring in the last few hundred seconds prior to ignition. Figure borrowed from [43].	6
1.2	Illustration showing the regimes within the white dwarf. Note the ash plume (the mushroom-like shape drawn in red) which rises very quickly due to bouyancy, and escapes the core region. The rising ash plume induces intense small-scale turbulence due to RT and KH instabilities. Figure borrowed from [43].	7
2.1	Spatial and temporal scales of the white dwarf during the explosion process. Physical regimes and their corresponding computational modeling regimes are highlighted. The spatial scales range from the deflagration-controlling scales on the order of the size of the white dwarf, down to the viscous dissipation scale. DDT occurs on scales slightly larger than the viscous dissipation scale. See text for details.	10
2.2	Critical length of hotspot region versus density for two nuclear energy release rates (4×10^{17} ergs g^{-1} , circles; 3×10^{17} ergs g^{-1} , triangles). Figure borrowed from [28]. . .	13
2.3	Pseudocolor plots of the induction time variable from three three-dimensional simulations of homogeneous and isotropic turbulence in a periodic domain (figure borrowed from [16]). The three plots differ in the degree of compressibility of the forcing, with the compressibility of the drive being (a) solenoidal, or divergence-free, (b) 0.75 percent compressive, and (c) 0.875 percent compressive.	15
3.1	Evolution of a synthetic hotspot, model GMdHtA08R130, with $A = 0.08$ and $R = 1.3 \times 10^4$ cm that results in a deflagration. Numerals 1 through 7 in the annotations refer to times $t_1 = 1.6$ ms, $t_2 = 1.65$ ms, $t_3 = 1.7$ ms, $t_4 = 1.75$ ms, $t_5 = 1.8$ ms, $t_6 = 1.825$ ms, and $t_7 = 1.85$ ms, respectively. Highlighted portions of the temperature, Mach number, pressure, and carbon abundance are shown at each time.	26
3.2	Evolution of a synthetic hotspot, model GMdHtA08R140, with $A = 0.08$ and $R = 1.4 \times 10^4$ cm that results in a detonation. Numerals 1 through 7 in the annotations refer to times $t_1 = 1.6$ ms, $t_2 = 1.65$ ms, $t_3 = 1.7$ ms, $t_4 = 1.75$ ms, $t_5 = 1.8$ ms, $t_6 = 1.825$ ms, and $t_7 = 1.85$ ms, respectively. Highlighted portions of the temperature, Mach number, pressure, and carbon abundance are shown at each time.	28
3.3	Space-time diagrams of the compressive and reactive waves in both a non-detonation-forming case (top; model GMdHtA08R130) and a detonation-forming case (bottom; model GMdHtA08R140). The times t_1 through t_7 are labeled in red for added context. .	29
3.4	Phase diagram illustrating the dependence of the ability of a hotspot to form a detonation as a function of amplitude and width, at a fixed ambient density and temperature of $\rho_{amb} = 1 \times 10^7$ g cm^{-3} and $T_{amb} = 1.78 \times 10^9$ K (dataset GMdHt) respectively. Three regions are identified: volumetric burning, carbon deflagration, and carbon detonation.	30

3.5	Critical conditions for DDT obtained by DNS of synthetically generated hotspot configurations. Shown are the contour lines separating the non-detonation-forming and detonation-forming regions of the reactive versus sound-crossing timescale plane for five databases of varying ambient density and temperature.	31
3.6	Evolution of a turbulence extracted hotspot, model <code>TEta17159tm21591rd00344</code> , that results in a detonation. Numerals 1 through 7 in the annotations refer to times $t_1 = 60.1$ ms, $t_2 = 110.1$ ms, $t_3 = 120.1$ ms, $t_4 = 130.1$ ms, $t_5 = 140.1$ ms, $t_6 = 150.1$ ms, and $t_7 = 160$ ms, respectively. Highlighted portions of the temperature, Mach number, pressure, and carbon abundance are shown at each time.	33
3.7	Evolution of a turbulence extracted hotspot, model <code>TEta16760tm21298rd00594</code> , that results in a detonation. Numerals 1 through 7 in the annotations refer to times $t_1 = 0$ ms, $t_2 = 120$ ms, $t_3 = 140$ ms, $t_4 = 150$ ms, and $t_5 = 160$ ms, respectively. Highlighted portions of the temperature, Mach number, pressure, and carbon abundance are shown at each time.	34
3.8	The <code>TE</code> dataset on the reactive versus sound-crossing timescale plane, separated into two panes with the left pane showing the bivariate histogram of non-detonation-forming points and the right pane showing the same but for the detonation-forming points. The colorscale indicates the probability of a point corresponding to that bin. Shown with a dotted red line is the contour from the <code>GMdHt</code> dataset for reference. . . .	35
3.9	Comparison of maximum Mach number reached versus r_s for ambient densities of $\rho_{\text{amb}} = 7.5 \times 10^6$ g cm $^{-3}$ (red squares), $\rho_{\text{amb}} = 1.0 \times 10^7$ g cm $^{-3}$ (gold right-arrows), and $\rho_{\text{amb}} = 1.33 \times 10^7$ g cm $^{-3}$ (green left-arrows), and for four normalized amplitudes: $A = 0.04$ (top left), $A = 0.08$ (top right), $A = 0.12$ (bottom left), and $A = 0.16$ (bottom right).	37
4.1	Normalized inputs from eight randomly chosen training samples. Shown in each panel is the normalized induction time (red circles), density (gold right-arrows), soundspeed (green left-arrows), velocity (blue squares), and z value (purple crosses).	42
4.2	Overview of the neural network approach for the naive strategy, <code>N1</code> . The network input is the induction time profile computed via DNS, but coarsened to the Δ_{tb} cutoff resolution. The binary classification labels of ‘no detonation’ and ‘detonation’ are determined by the result of the corresponding DNS.	44
4.3	Traing and validation loss (top panel) and accuracy metrics (bottom panel) for the <code>N1</code> model trained on the synthetic dataset, dataset <code>td.naive.synthetic</code>	48
4.4	Comparison of the training and validation loss for the <code>N2</code> (top left panel), <code>N3</code> (top right panel), <code>N4</code> (bottom left panel), and <code>N5</code> (bottom right panel) models on the <code>td.naive.turb</code> dataset.	50
4.5	Comparison of the AUC metric on the training and validation data for the <code>N2</code> (top left panel), <code>N3</code> (top right panel), <code>N4</code> (bottom left panel), and <code>N5</code> (bottom right panel) models on the <code>td.naive.turb</code> dataset.	51

4.6	Weights for filters 1 – 8 of the first layer of model $\mathbb{N}2$ are plotted, with each row comprising one filter and the individual kernels for inputs of induction time, density, soundspeed, and velocity spanning the columns. For plotting convenience, weights are normalized across filters for each input channel.	52
4.7	Training and validation performance of the $\mathbb{K}1$ model trained on the synthetic dataset, dataset <code>td.khokhlov.synthetic</code> . The network achieves a very high Accuracy score for the training (thick solid black line) and validation (thick dotted black line) datasets. Also the AUC score is near the maximum score possible of 1 for both datasets (thin solid blue line and thin dotted blue line).	53
4.8	Training and validation performance of the $\mathbb{K}2$ model trained on the turbulence extracted dataset, dataset <code>td.khokhlov.turb</code>	54
4.9	Overview of 1D turbulence used for verification studies. Shown is the probability density of velocities collected over 125 time samples (top left panel); the kinetic energy spectrum (top right panel) collected over the same number of samples, compensated by multiplying with $k^{5/3}$, where k is the wavenumber; the evolution of the RMS Mach number (middle left panel) the three velocity components (middle right panel), and the mean and maximum temperature (bottom left panel); and finally a bivariate histogram of amplitudes and widths of temperature fluctuations (bottom right panel) with higher frequency indicated by darker color.	55
4.10	Results of the verification process for the naive model $\mathbb{N}2$. Shown are the network predicted detonation probabilities (shown in color) on the δ_t - δ_x plane.	56
4.11	Results of the verification process for the Khokhlov model $\mathbb{K}2$. Shown are the network predicted detonation probabilities (shown in color) on the δ_t - δ_x plane.	57
4.12	Convergence of network accuracy with the number of training samples.	59
A.1	Statistics of temperature perturbations near the end of the self-heating phase in three-dimensional reactive turbulence simulations. The distributions are categorized into four temperature ranges.	62
A.2	Histograms of the calculated amplitude (left panel) and standard deviation (right panel) of the fitted functions to the turbulence extracted profiles.	63
A.3	Histogram of the R^2 goodness-of-fit statistic for the fitted functions to the turbulence extracted profiles.	64

LIST OF SYMBOLS

t	time
x	spatial coordinate
S_L	the laminar flame speed
τ	induction time
u_{sp}	reactive wave speed
z	reactive wave speed normalized by local soundspeed
c	speed of sound
D_{CJ}	velocity of a Chapman-Jouget detonation
ρ	density
ρ_{amb}	ambient density
T_{amb}	ambient temperature
$\delta\rho$	amplitude of density perturbation
R	width of density perturbation
A	normalized amplitude of density perturbation
u	velocity
p	pressure
\mathbf{X}	species concentrations
X_f	fuel concentration
\mathbf{R}	species reaction rates
\dot{Q}	nuclear energy generation term
Δx	mesh resolution
N	number of computational cells
\mathbf{U}	approximate solution
$\hat{\mathbf{F}}$	numerical fluxes
$\hat{\mathbf{S}}$	numerical source terms
ϕ	exact solution
r_0	radius of hotspot region
r_s	distance from the center of the hotspot to the point where the reactive wave speed equals the soundspeed
r_s^*	the critical value of r_s below which detonation cannot occur
σ_0	standard deviation of induction times in hotspot region
c_0	soundspeed in hotspot region
ε	threshold for defining size of hotspot region
Δ_{wd}	ILES filter cutoff for the full-star explosion scale of the white dwarf
Δ_{tb}	ILES filter cutoff for the turbulence-in-a-box scale
q	actual label of a neural network input sample
\hat{q}	predicted label of a neural network input sample
χ	data of a neural network input sample
φ	activation function
b	layer biases
w	layer weights
ℓ	network layer number
n_s	number of training samples
n_x	number of spatial points in the input data
n_{ch}	number of input channels in a convolutional network
δ_t	time delay between network prediction and actual detonation
δ_x	spatial distance between location where network prediction made and estimated detonation origin

ABSTRACT

A novel, data-driven model of deflagration-to-detonation transition (DDT) is constructed for application to explosions of thermonuclear supernovae (SN Ia). The DDT mechanism has been suggested as the necessary physics process to obtain qualitative agreement between SN Ia observations and computational explosion models. This work builds upon a series of studies of turbulent combustion that develops during the final stages of the SN explosion. These studies suggest that DDT can occur in the turbulized flame of the white dwarf via the Zel'dovich reactivity gradient mechanism when hotspots are formed. We construct a large database of direct numerical simulations that explore the parameter space of the Zel'dovich initiated detonation. We use this database to construct a neural network classifier for hotspots. The classifier is integrated into our supernova simulation code, FLASH/Proteus, and is used as the basis for a subgrid-scale model for DDT. The classifier is evaluated both in the training environment and in reactive turbulence simulations to verify its accuracy in realistic conditions.

CHAPTER 1

INTRODUCTION

1.1 Motivation and outline

The rapid transition of a subsonic flame, also known as a deflagration, to a supersonic and more energetic detonation can occur suddenly in numerous industrial scenarios including, but not limited to, fuel transportation [9], hazardous chemical storage [47], and loss-of-cooling incidents in nuclear reactors with H₂-air-steam mixtures [30]. This phenomenon is known as the deflagration-to-detonation transition (DDT), and it is a topic of active research in the combustion community. While a DDT in the aforementioned instances may have devastating effects, the phenomenon can also be utilized for constructive purposes in engineering applications. For example, DDT can be exploited in pulse detonation engines as an alternative to direct detonation initiation [51].

Beyond terrestrial applications, DDT is suspected to have contributed to the makeup of the universe through the process of nucleosynthesis during thermonuclear stellar explosions, also known as supernovae (SNe). These fascinating events result in the release of an enormous amount of energy; on the order of 10^{51} erg. The exact mechanism of the explosion is not yet entirely understood. This dissertation aims to provide a computational model for the possible DDT in thermonuclear SNe.

In this chapter the reader is provided with a brief introduction to the basic combustion physics relevant to DDT and to the topic of thermonuclear explosions. Chapter 2 reviews the prior work done in modeling the deflagration-to-detonation transition in thermonuclear SNe and provides an overview of the modeling approach used in the present work. In Chapter 3 the critical conditions for detonation initiation are investigated. Chapter 4 introduces a novel, data-driven approach to subgrid-scale (SGS) modeling of DDT. Concluding remarks are provided in Chapter 5, as well as a critical discussion of the aspects of the present work that can be improved or expanded upon.

1.2 Relevant combustion physics

The deflagration-to-detonation transition requires the presence of combustion waves. Combustion waves are defined by a perturbation in fuel consumption rate and energy release propagating through a fuel mixture. Several viable conditions for the idealized, one-dimensional combustion

wave are described by the well-known Rankine-Hugoniot relation (see Chapter 4 of [32]). In particular, the weak deflagration and the detonation are the two modes of combustion most frequently encountered in actual physical systems.

The deflagration is characterized by a subsonic propagation velocity. The deflagration front results in an increase in fluid velocity, and a mild decrease in gas density and pressure. The velocity of a one-dimensional deflagration is known as the laminar flame speed, S_L , and it is determined by thermal conduction and mass diffusion [32].

The detonation is a supersonic mode of combustion that has a shock-reaction structure. The first theoretical descriptions of the one-dimensional detonation wave were provided independently by Chapman [46] and Jouget [25]. While the Chapman-Jouget (CJ) solution is fairly accurate, it considers the reaction zone as infinitesimally thin, whereas in reality the reaction zone has some finite width.

A more detailed description of the detonation wave was provided by Zel'dovich [57], von Neumann [60] and Döring [14] (ZND). The ZND model describes the one-dimensional detonation as a leading shockwave with a narrow reaction zone behind it. The shockwave serves to compress the upstream fuel, rapidly raising the temperature, pressure, and density closer to the point of ignition. The reaction zone behind the shockwave can be divided into two regions: the induction zone and the reaction zone. The induction zone is a region inside which induction times, the estimated amount of time for the fuel in a small mass element to burn, and reaction rates are both low. In the reaction zone, reaction rates increase substantially away from the shockwave. In a self-sustaining detonation, the reaction zone is responsible for a significant amount of thermal pressure due to the energy release. This thermal pressure acts like a piston behind the leading shockwave, propelling the shockwave into the unburnt region.

The initiation of a detonation requires the coupling of a compressive wave and a reactive wave. If a sufficiently strong ignition source is present a detonation can be directly initiated [1]. This source must ignite the fuel and provide a strong shockwave. Such a strong ignition source is rarely present in nature, yet detonations are known to arise nevertheless. Another means of detonation initiation was proposed by Zel'dovich et al. [62] via the mechanism of *spontaneous propagation*.

1.2.1 Spontaneous detonation

Consider a region of fuel in one-dimensional space with a nonuniform distribution of the induction time field, $\tau(x)$, where x is the spatial coordinate. Such regions are referred to hereafter as

‘hotspots’. The nonuniform spatial profile in the induction time gives the potential for a ‘spontaneous’ wave due to the successive release of energy as each mass element undergoes burning and energy release. This wave is independent of the soundspeed and thermal conductivity of the gas. The phase velocity of the spontaneous wave is given as

$$u_{sp} := \left(\frac{\partial \tau}{\partial x} \right)^{-1}. \quad (1.1)$$

This relation indicates that regions of low induction time gradient have a higher phase velocity and vice versa.

For a shock-reaction complex to form, both a compressive and reactive wave must coexist for some period of time to allow the feedback mechanism to strengthen (and steepen) the compressive wave. The velocity of the compressive wave is primarily governed by the soundspeed, c , but the compressive wave may also be accelerated by overpressure due to burning behind it. Meanwhile, the speed of the emerging reactive wave is governed primarily by Equation (1.1). Thus, the speed of the reactive wave should be in the vicinity of the local soundspeed if a coupled burning process is to have any chance of formation.

Zel’dovich [61] describes several regimes of spontaneous propagation. These regimes have also been neatly summarized in the textbook of Kuo [32], and they are only briefly reviewed here. Given the speed of a CJ detonation, D_{CJ} , the regimes are given by:

1. If $u_{sp} > D_{CJ}$, the result is an under-driven detonation wave. In the limit $u_{sp} \rightarrow \infty$ this case corresponds to a constant-volume explosion.
2. If $u_{sp} \leq D_{CJ}$ then a shock wave can form ahead of the reactive wave and ultimately transform into a detonation through the feedback process.
3. If $S_L < u_{sp} \ll c < D_{CJ}$, then a weak deflagration wave is formed which travels faster than the laminar flame speed.
4. If $u_{sp} < S_L$, then a deflagration forms which travels at the laminar flame speed.

Essentially, if the magnitude of u_{sp} is too large, then the successive energy release happens on a timescale smaller than the acoustic timescale such that no coupled feedback mechanism can occur. Too small, and the acoustic wave will outrun the reactive wave, leaving either a slightly overdriven deflagration or a deflagration travelling at speed S_L .

The aforementioned regimes are adequate to describe only the most simple initial hydrodynamic states and do not consider either the initial hydrodynamic state or complex thermo-fluid dynamics,

as Zel'dovich himself points out. In an effort to compensate for these effects the authors of [19] introduce a *range* of critical reactivity gradients which may lead to detonation in their analysis of hotspots in chemical fuel mixtures. Similarly, the existence of critical reactivity gradient values was also suggested in a large numerical study by Oran & Gamezo [45]. The authors suggest that the reactivity gradient mechanism has some ‘universality’ across many regimes and mixtures.

Numerous experimental studies have examined the process of DDT, and some of these have provided evidence in support of the role of the reactivity gradient mechanism in detonation formation. Urtiew, Oppenheim, & Saunders [59] studied the transition to detonation of flames inside of a long enclosed tube. Lee, Knystautas, & Yoshikawaet [33] studied detonations initiated via a photochemical energy source and found that a certain range of gradient values are necessary for the shock wave to amplify and form a detonation. For a useful review of the spontaneous detonation of hotspots covering the mathematical, experimental, and computational modeling frames of reference, see [6].

While laboratory experiments have managed to initiate detonations either by boundary-induced turbulence or direct initiation methods, the formation of detonations in *unconfined* turbulence does not occur as readily. The mechanism that is believed to lead to the formation of detonation-prone, nonuniformly heated regions in unconfined settings is discussed next. This mechanism is known as flame acceleration.

1.2.2 Flame acceleration

The process of flame acceleration is essential for the deflagration-to-detonation transition in an unconfined setting. There are numerous mechanisms which can cause a laminar flame to become turbulent. In confined settings, surface roughness or obstacles typically play a significant role (see [54]). Without solid boundaries however, turbulence can occur along the flame surface due to hydrodynamic instabilities such as Rayleigh-Taylor (RT) or Kelvin Helmholtz (KH) instabilities, or it can be generated by the intrinsic flame instability at the flame surface itself [54]. Turbulence can significantly modify the structure of the laminar flame front depending on its intensity and length scales. Higher local reaction rates, flame speeds, and enthalpy can be achieved in areas with a high degree of flame stretching, or curvature.

The turbulent flame can be classified into at least five distinct regions [54] based on the ratios of the velocity and characteristic length scales of turbulence to those of the laminar flame. As mentioned, the *laminar flame regime* is rarely achieved in natural settings due to various instabilities.

If the velocity fluctuations are small, and the turbulent length scales are large with respect to the flame thickness, then the flame is only gently distorted by the velocity field. This regime is known as the *wrinkled flame regime*.

As the turbulent velocity fluctuations increase, the length scales tend to become smaller, and the disturbances to the flame become more pronounced. This has the effect of increasing the strain on the flame surface. If the flame surface remains unbroken, then this regime is referred to as the *corrugated flame regime*. When the smallest eddies become comparable to the flame thickness they can enter and broaden the preheat zone [49]. This regime is known as the *thin reaction zone*. These regimes result, to varying degrees, in increased flame surface area, but more importantly in strain rate effects that further increase flame velocities.

Then there is a regime in which turbulent eddies shatter the flame surface. This regime, known as the *distributed reaction zone*, is realized when the timescale of the turbulent eddies is smaller than the timescale of the burning. In other words, eddies are able to mix the flame surface with the upstream fuel more quickly than the flame can burn away the eddy. This has important consequences for the existence of hotspot regions.

1.3 Thermonuclear supernova explosion scenario

The evolution of a main sequence star such as the Sun draws to an end when its hydrogen and helium fuels have been exhausted, leaving behind an extremely dense, hot, electron degenerate plasma core known as a white dwarf (WD) star [22]. In this final stage of the star's evolution, the WD slowly burns its remaining carbon and oxygen fuels over a period of several billion years as the star gently cools. The thermal pressure due to the mild burning of carbon, as well as the electron degeneracy pressure serve to resist the weight of the material in the outer layers, keeping the star in hydrostatic equilibrium.

If a WD is in a close binary system then there is the potential for an enormous and rapid release of energy via a thermonuclear explosion. There are two accepted progenitor systems: single degenerate (SD), consisting of a WD and a non-degenerate main sequence giant star, and double degenerate (DD), consisting of two degenerate, intermediate mass white dwarves.

In the SD scenario, the interior of the rotating WD is mostly composed of carbon and oxygen (C/O) fuel due to the burning of hydrogen. This C/O core experiences compressive heating due to the massive outer layers, but also radiative cooling. While these forces are closely balanced for some

time, there is a trend toward heating in the star that lasts for centuries due to the accumulation of mass from the donor star [63]. This phase is known as the “simmering” phase. When the radiative cooling processes are no longer able to cool the star, convection in the core is thought to take over. Eventually, the core temperature rises to a point where ignition of carbon takes place, and a runaway process begins. The convection during the simmering stage was studied by Nonaka et al. [43], and the authors observed the evolution of temperature as shown in Figure 1.1. In this

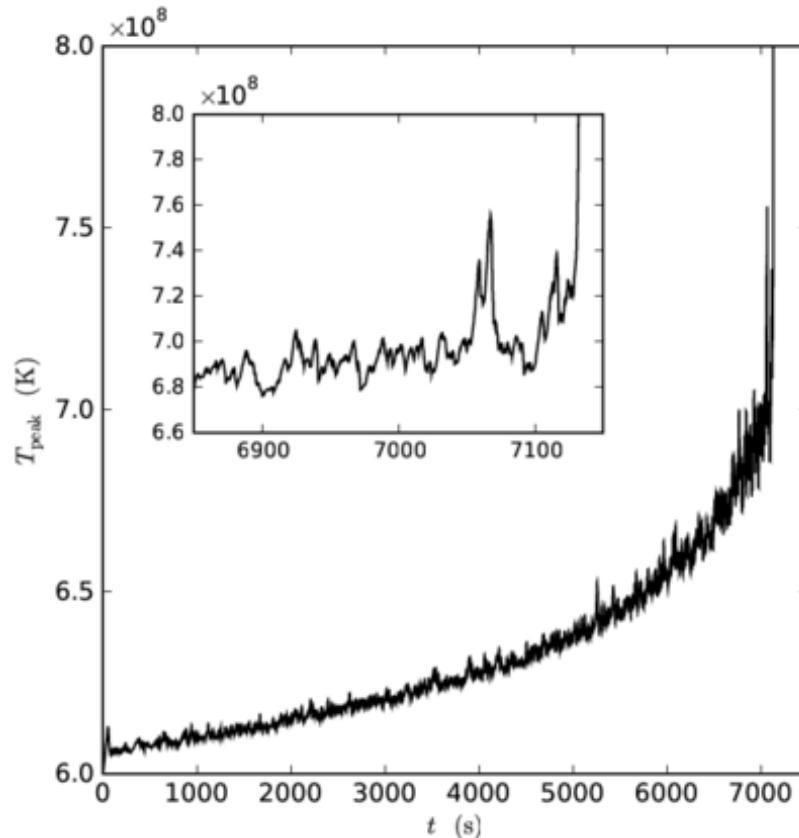


Figure 1.1: Simulated evolution of peak temperature within the core region of a white dwarf up to the moments of ignition. The inset shows the rapid temperature rise occurring in the last few hundred seconds prior to ignition. Figure borrowed from [43].

study the peak temperature in the system rapidly rises within a matter of minutes (note the scale of the inset of Figure 1.1).

It is supposed that the ignition occurs at one or more regions near the core. The location of the first ignition within the star is important in determining the observational characteristics of the explosion [39]. Whether the first ignition occurs in the center of the core or off-center has been debated in the literature. An off-center scenario has been determined to be most likely in

several works [40, 43]. After ignition, ash plumes (also referred to as flame “bubbles”), rise toward the surface of the star due to bouyancy forces. An illustrative diagram is borrowed from [43] and included here in Figure 1.2. The rapidly rising plume is unstable to Landau-Darrieus, Rayleigh-

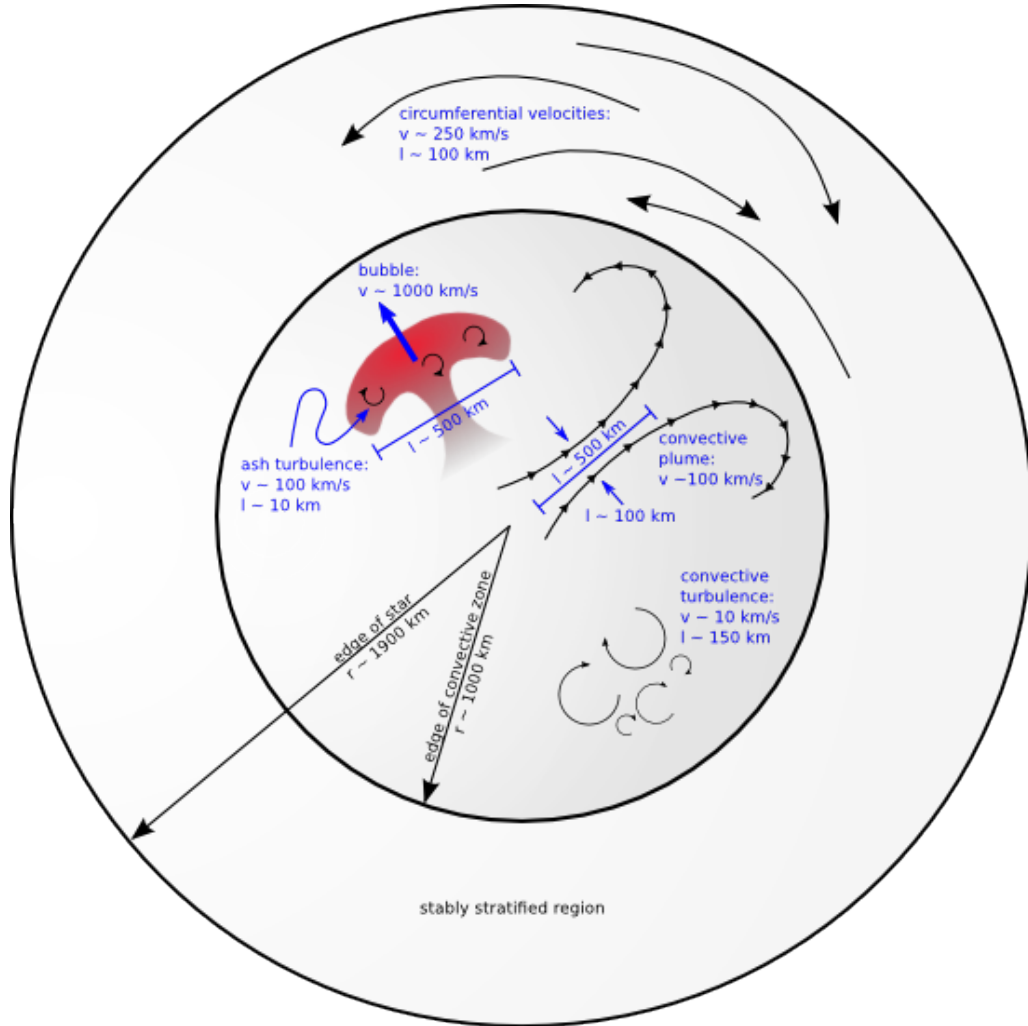


Figure 1.2: Illustration showing the regimes within the white dwarf. Note the ash plume (the mushroom-like shape drawn in red) which rises very quickly due to bouyancy, and escapes the core region. The rising ash plume induces intense small-scale turbulence due to RT and KH instabilities. Figure borrowed from [43].

Taylor, and Kelvin-Helmholtz instabilities [7]. The result is the generation of turbulence along the edges of the plume.

Turbulence along the surface of the hot ash plume mixes cold fuel from outside of the WD core with hot ash from inside the plume. The mixing between cold fuel and hot ash serves to warm the fuel, bringing it closer to the point of ignition. At this point it is speculated if a transition from

deflagration to detonation can occur. The so-called “delayed detonation” model was introduced by Khokhlov [26], arguing that spontaneous detonation (i.e. detonation powered by the Zel’dovich reactivity gradient mechanism) can occur within the turbulent regions of a deflagrating WD.

The delayed detonation model was proposed to address the inability of pure detonation models [3] or pure deflagration models [41] to match observations [28]. The pure detonation model is known to produce an insufficient amount of intermediate mass elements [26], while the pure deflagration models tend to produce an insufficient amount of energy, evidenced by an excess of ^{54}Fe [42].

The spectral properties of the ejecta of delayed detonation models were investigated in [24]. Other theories have also been proposed. Plewa et al. [50] introduced the gravitationally confined detonation model, which posits that after an off-center ignition, the resulting ash plume bursts through the surface layers, and a mix of cold fuel from the stably stratified region, and hot ash from the plume converge at a point opposite from the surface burst location. The converging flow is supersonic, and the interaction between shockwaves and the hot fuel has been shown to produce a detonation in computational models.

Even though these models may be successful at qualitatively matching observations, it is important to point out that their maximum resolution (usually on the 1×10^5 cm scale) is not resolving anywhere near the DDT-controlling scales. The actual SGS conditions in all of these scenarios are largely unknown. To date, a criteria that can predict the onset of DDT in Type Ia SNe is not available. There remains a significant degree of uncertainty about the turbulent conditions during the deflagration phase.

Even if the large-scale conditions are known, the accurate modeling of flame-turbulence interactions on smaller scales is challenging [23]. Is a transition to detonation possible along the interface between cold fuel and hot ash from the rising plume? If so, what is the mechanism? Can this mechanism be parameterized? In this dissertation the available knowledge on these topics will be collected and a path toward a useful metric for predicting the onset of DDT will be proposed. Physical insights from the existing literature will be used to guide state-of-the-art, data-driven techniques.

CHAPTER 2

CHALLENGES OF MODELING THERMONUCLEAR SUPERNOVAE

2.1 Introduction

The primary limitation of computational models for SN Ia is the so-called “tyranny of scales”; that is to say that some physics processes are known to occur on very large spatial and temporal scales, while others may occur simultaneously on significantly smaller scales. For example, the characteristic size of turbulent eddies in the convectively unstable core is thought to range from hundreds of kilometers down to several centimeters. Likewise, the disparity in timescales between the large-scale convective motions and nuclear burning spans roughly seven orders of magnitude.

Figure 2.1 illustrates the extreme challenge of scales in this problem. The upper limit of the spatial range (the vertical axis in Figure 2.1) is defined by the radius of the WD, which is typically on the order of hundreds of kilometers (or about 10^8 to 10^9 cm). On slightly smaller scales, roughly 10^7 to 10^8 cm, the initial modes of the RT unstable deflagration plumes are determined. Once the star begins exploding, deflagration plumes travel toward the outer layer of the star where they expand and lose momentum (region 1). As the deflagration plumes expand outward they induce mixing between cold fuel and hot ash, producing turbulence (region 2). The energy from these large-scale motions is transferred to smaller scales through the turbulent energy cascade. Eddies larger than the Gibson scale [48] are able to distort the flame surface with their momentum before they burn away (region 3), while smaller eddies are not (region 4). The Gibson scale is a function of the laminar flame speed and thus decreases during the evolution as density decreases (line separating regions 3 and 4). Meanwhile, the flame thickness increases with decreasing density. At the point where the spatial scales of the Gibson scale and the flame thickness become comparable (region 5), the distributed burning regime is entered. In this regime, DDT is thought to be most probable.

On the right side of the diagram in Figure 2.1 the physics regime is summarized in one column, and the simulation regime in the other. The scales between roughly 10^7 cm and 10^9 cm are defined as the deflagration-controlling scales. On these scales, the star’s radius, compositional makeup, Atwood number (a dimensionless ratio of densities across an interface), and other properties deter-

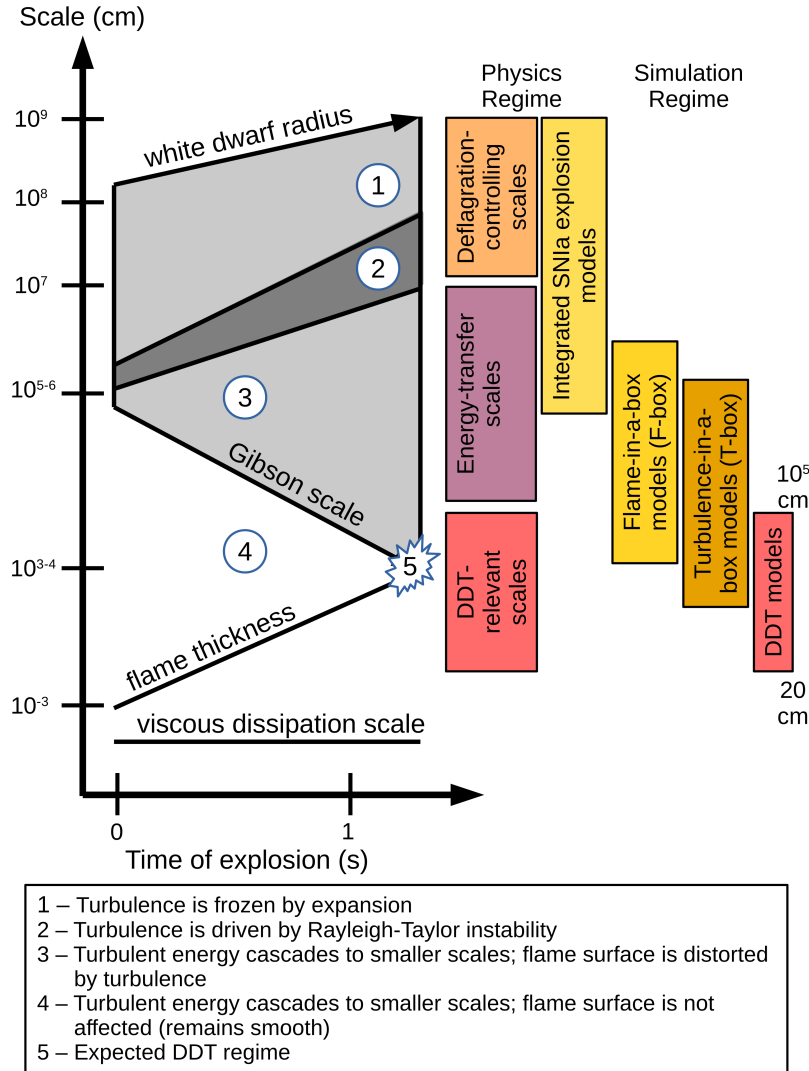


Figure 2.1: Spatial and temporal scales of the white dwarf during the explosion process. Physical regimes and their corresponding computational modeling regimes are highlighted. The spatial scales range from the deflagration-controlling scales on the order of the size of the white dwarf, down to the viscous dissipation scale. DDT occurs on scales slightly larger than the viscous dissipation scale. See text for details.

mine the characteristics of the deflagrating ash plume. Scales smaller than this range, from about 10^4 cm to 10^7 cm, can be considered as the energy-transfer scales in which turbulent kinetic energy cascades from large to small scales as per the theory of isotropic turbulence [31]. Below these scales are the scales relevant to DDT, from the viscous dissipation scale of about 10^{-3} cm to 10^4 cm.

Unfortunately the ability to resolve the roughly 10 orders of magnitude separating the spatial

scales in the WD explosion is currently technologically out of reach. The only feasible solution at present is to consider smaller computational domains. In the right text column of the figure, four simulation regimes are introduced: the full-star explosion model, the flame-in-a-box models which study the RT deflagration plumes, the turbulence-in-a-box models, which study finer details within the flame brush of the RT deflagration plume, and finally the direct numerical simulation of detonation formation. In particular the turbulence-in-a-box models study how hotspot regions can form and possibly detonate.

The approach by other researchers in the computational astrophysics community is not dissimilar from the present one. Typically either the full star is modeled and turbulence and/or flame physics are handled by scaling relations or SGS models such as in [10], or the flame physics on smaller scales are solved directly [5] in order to better design SGS models or refine model parameters for full-star models. The hope by researchers is that the manual iteration back and forth between full-star models and micro-physics models may achieve convergence on some aspects of the problem.

2.2 Modeling of DDT

As discussed in Chapter 1, the pure deflagration and pure detonation models of Type Ia SNe are both known to produce discrepancies with observations. This has led researchers to consider delayed detonation models, among others. In the delayed detonation scenario, again, DDT is suspected to occur when the ash plume breaks out of the core region of the star.

According to Kohkhlov, Oran, & Wheeler [28], determining whether a transition can occur in this scenario basically amounts to (1) determining which characteristics allow a hotspot to form a self-sustaining detonation wave via the Zel’dovich reactivity gradient mechanism, and (2) whether the outgoing ash plume and subsequent reactive turbulence can produce hotspots with those characteristics.

2.2.1 Conditions for the transition to detonation

Several prominent works that produced some estimates of the conditions necessary for a hotspot to spontaneously produce a detonation wave are now briefly reviewed. As discussed in Chapter 1, one of the earliest analytical works is by Zel’dovich et al. [62] in which the authors determine critical gradients of temperature for an initially linear temperature profile in a chemical gas mixture. In the context of thermonuclear flames, Khokhlov [27] studies the evolution of hotspots using a statistical

approach. In his work the initial conditions and evolution of temperature and induction time are described by a distribution function.

One of the key results of this work is the description of the necessary condition for detonation initiation in a region of size r_0 as

$$\sigma_0 < \frac{r_0}{\alpha \cdot c} \quad (2.1)$$

where σ_0 is the standard deviation of induction times in the region, c is the soundspeed in the region, and α is a parameter that in general depends on the background conditions and turbulence. On the right-hand side of Equation (2.1) is the approximate sound-crossing time within the region r_0 . The sound-crossing time is the amount of time it takes a soundwave to travel a specified distance. On the left-hand side, is the variation in induction times. This value is indicative of the reactive wavespeed, as a smaller amount of variation necessarily implies that the ‘mini-explosions’ are better synchronized in time. Better synchronization in time leads to a faster phase velocity of the spontaneous wave and a better opportunity for coupling to occur between the reactive and compressive waves.

What Khokhlov argues via Equation (2.1) is that the reactive timescale given by the variation in induction times σ_0 must be approximately less than the sound-crossing time of the region in order for a detonation to occur. If this condition is not satisfied then too much of the energy produced via burning can escape the region in the form of acoustic energy for the coupling process to become self-sustaining.

The previously mentioned work of Khokhlov, Oran, & Wheeler [28] analyzed hotspot configurations with linear profiles in fuel concentration, each beginning with zero fuel abundance at the center of the region, and reaching the ambient abundance at some length, L . The assumption of linearity of the fuel concentration is a simplistic model of the situation in which cold fuel and hot ash mix. In the study, the length of the perturbed region is varied along with the density in order to determine the critical length and its dependence on density. The results of this work are summarized in Figure 2.2. The figure indicates that the critical length required for detonation decreases with increasing density. The authors attribute this to the specific heat of the matter being lower at higher densities, meaning that less heat is required to raise the temperature of the fuel toward ignition.

A later study by Seitenzahl et al. [52] investigated in much more detail the formation of spontaneous detonations from hotspots in the context of SN Ia. Their study introduced several

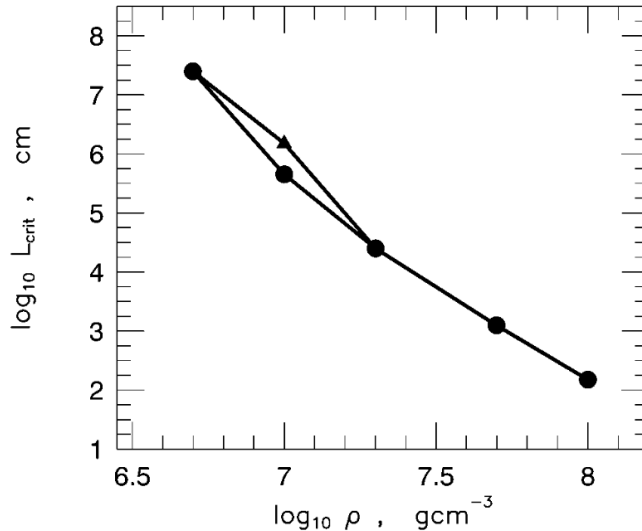


Figure 2.2: Critical length of hotspot region versus density for two nuclear energy release rates (4×10^{17} ergs g^{-1} , circles; 3×10^{17} ergs g^{-1} , triangles). Figure borrowed from [28].

novel aspects to the modeling of hotspots: a variety of initial temperature profiles, including linear (as in [28]), exponential, Gaussian, and several non-physically motivated profiles; grid convergence studies; and some consideration of multi-dimensionality.

The estimates by Khokhlov et al. of the critical size for a mixed region to produce a detonation were used as constraints in the construction of a SGS model for DDT in the context of SN Ia by Ciaraldi-Schoolmann, Seitenzahl, & Röpke [10]. The authors' model also incorporates estimated constraints on the turbulent velocity fluctuations, fuel composition, density, and fractal characteristics of the flame surface known to produce DDT. These quantities are computed on the resolved scale.

2.2.2 Turbulent conditions in the deflagrating white dwarf

Whether the properties of the reactive turbulence in the deflagrating WD can support the formation and survival of hotspot regions long enough for them to form detonation waves is still somewhat of an open question. In fact, not only must these hotspot regions remain unperturbed for some time following their formation, but they must contain a significant amount of fuel as well. Questions related to the formation of hotspots on scales relevant to DDT have been investigated in a few works.

Lisewski, Hillebrandt, & Woosley [35] investigated the ability of small-scale turbulence with varying densities and velocity fluctuations to create detonations. The authors found detonations to occur at turbulent velocity fluctuations of between $0.5 \times 10^8 \text{ cm s}^{-1}$ and 10^8 cm s^{-1} depending on the density and fuel composition.

Niemeyer & Woosley [39] argue that the existence of sufficiently large hotspot regions with preferable induction time gradients is unlikely. The authors conclude that if viable hotspots are created at all, they likely occur once the deflagration enters the distributed burning regime.

2.2.3 Modeling domains

As described in Chapter 1, it is not feasible to resolve all of the relevant spatial scales in a single simulation. The preferred strategy for modeling is to decompose the problem into smaller problem domains, with each domain attempting to model a particular physics process.

Full-star explosion models. The largest scale range is the full-star. The full star model simulates from the end of the carbon ‘simmering’ phase prior to the thermal runaway in the convective core to the subsequent explosion. Due to the limited resolution in this type of large scale model, it is common to manually ignite a parcel of fluid in either the core region (central ignition) or in the RT flame plume (delayed ignition). This problem setup is given the name `wd` (short for white dwarf). In the context of the ILES approach, the cutoff length is defined as Δ_{wd} . This value is typically near 10^5 cm .

Rayleigh-Taylor deflagration models. At the intermediate spatial ranges, a single deflagration bubble of the exploding WD is modeled to determine the turbulent kinetic energy and scales of the turbulent driving in the flame brush. This problem setup is referred to as `flame-in-a-box`. In this model the cutoff length is denoted by Δ_{rt} , and the value in the highest resolved cases is on the order of 10^3 cm .

Reactive turbulence simulations. Further refining the model range, the turbulent conditions in the flame brush may be examined more closely. In a problem setup referred to as `tburn`, the conditions in the flame brush are emulated in a three-dimensional periodic cube domain with a length of $32 \times 10^5 \text{ cm}$ on each side. The filter cutoff scale in these models is typically set to $\Delta_{\text{tb}} = 3.125 \times 10^3 \text{ cm}$. The turbulence is generated numerically with a spectral driving routine [15]. The degree of compressibility of the drive ranges from purely solenoidal (divergence-free) or purely compressible (curl-free). A comparison of the nature of turbulence for different driving

compressibility values in the `tburn` models [16] is shown in Figure 2.3, These models are useful for

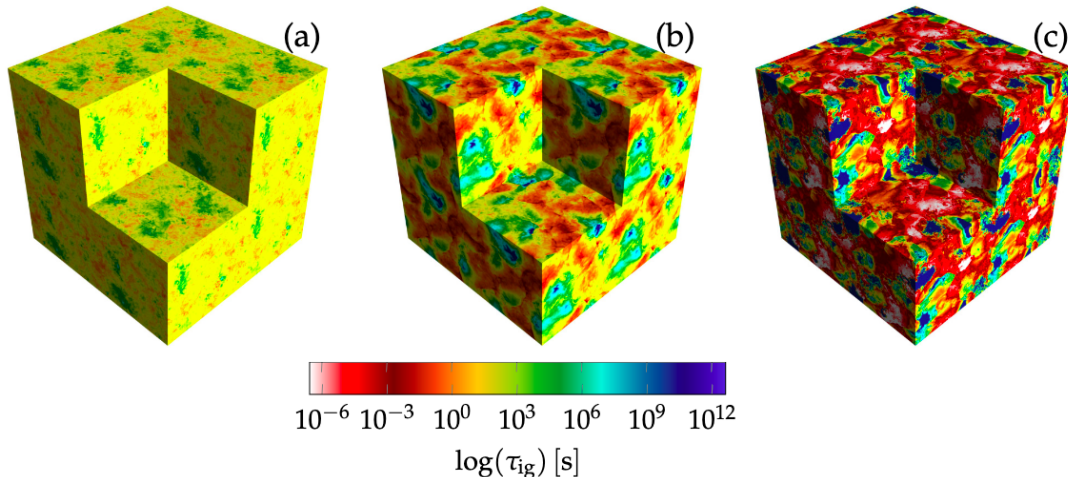


Figure 2.3: Pseudocolor plots of the induction time variable from three three-dimensional simulations of homogeneous and isotropic turbulence in a periodic domain (figure borrowed from [16]). The three plots differ in the degree of compressibility of the forcing, with the compressibility of the drive being (a) solenoidal, or divergence-free, (b) 0.75 percent compressive, and (c) 0.875 percent compressive.

modeling the small scale perturbations in induction time and pressure that may lead to deflagrations, hotspots, and either shock-initiated detonations, or detonation initiation via the Zel’dovich mechanism [8].

Direct numerical simulation. Direct numerical simulation may be used if even finer resolution of the turbulence-flame interaction is desired, or if more accuracy is required in studies of hotspot detonation formation. Notably, the resolution of Δ_{tb} is low for resolving detonation formation.

2.3 Computational modeling

In this work, the Euler equations are used to model compressible, reactive flows:

$$\rho_t + \nabla \cdot (\rho \mathbf{u}) = 0, \quad (2.2a)$$

$$(\rho \mathbf{u})_t + \nabla \cdot (\rho \mathbf{u} \mathbf{u}^T + p \mathbf{I}) = \mathbf{0}, \quad (2.2b)$$

$$(\rho \mathbf{X})_t + \nabla \cdot (\rho \mathbf{X} \mathbf{u}) = \mathbf{R}, \quad (2.2c)$$

$$(\rho E)_t + \nabla \cdot (\rho E + p) \mathbf{u} = \dot{Q}, \quad (2.2d)$$

where ρ is the mass density of the gas mixture, \mathbf{u} is the velocity vector, p is the pressure, E is the specific total energy, \mathbf{X} is the vector of species mass fractions, \mathbf{R} is the vector of species reaction rates, and \dot{Q} is the energy source term. The mass fraction for the i^{th} species can be written as $X_i = \rho_i/\rho$, where ρ_i is the corresponding mass density, meaning that the species must collectively satisfy the constraint $\sum_{i=1}^{\mathcal{N}_{\text{species}}} X_i = 1$, where $\mathcal{N}_{\text{species}}$ is the number of species considered. A special notation, X_f , is used for the abundance of carbon fuel.

The total specific energy is calculated as the sum of the specific internal energy and the kinetic energy as $E = e + \frac{1}{2}\mathbf{u}\mathbf{u}^T$. The above system of PDEs is closed using a suitable EoS which relates the pressure to density, internal energy, and composition.

2.3.1 Finite volume discretization

The system of partial differential equations Equation (2.2) are discretized using the standard finite volume (FV) approach. Given a uniform discretization of the domain $x \in [x_a, x_b]$ with cell size $\Delta x = (x_b - x_a)/N$, where N is the number of cells, the following one-dimensional semi-discrete scheme is considered:

$$\mathbf{U}_i^{n+1} = \mathbf{U}_i^n - \frac{1}{\Delta x} \int_{t_n}^{t_{n+1}} \left(\hat{\mathbf{F}}_i - \hat{\mathbf{F}}_{i-1} \right) dt + \int_{t_n}^{t_{n+1}} \hat{\mathbf{S}}_i dt. \quad (2.3)$$

Here \mathbf{U}_i^n is an approximation to the average of the exact solution, which is denoted as $bm\phi(x, t)$, in the control volume $[x_{i-1}, x_i]$ at t_n . The numerical flux approximates the exact flux function as

$$\hat{\mathbf{F}}_i := \hat{\mathbf{F}}(\mathbf{U}_{i-k}, \dots, \mathbf{U}_{i+k+1}) \approx \mathbf{F}(\phi(x_i, t)), \quad (2.4)$$

where $2k$ is the number of cells comprising the reconstruction stencil, and the term

$$\hat{\mathbf{S}}_i := \mathbf{S}(\mathbf{U}_i) \approx \frac{1}{\Delta x} \int_{x_{i-1}}^{x_i} \mathbf{S}(\phi(x, t)) dx \quad (2.5)$$

is an approximate average of the source term within the control volume. The fluxes and source terms may be handled separately in time using standard operator splitting approaches (see, [36], and references therein).

2.3.2 Multiresolution based adaptive mesh refinement

In this work the mesh is adapted using multiresolution (MR) based adaptive mesh refinement (AMR). The application of MR analysis to FV schemes was first introduced by Harten [21] to adaptively compute expensive flux calculations in simulations of compressible gas dynamics. Since then it has gained popularity and been used for designing fully adaptive schemes [11].

A (MR) analysis is a set of nested subspaces of $L^2(\mathbb{R})$ that forms an orthonormal basis for $L^2(\mathbb{R})$ [55]. An MR analysis $\{\mathcal{V}_j\}$ satisfies the relation

$$\mathcal{V}_0 \subset \mathcal{V}_1 \subset \mathcal{V}_2 \subset \dots \subset L^2. \quad (2.6)$$

By introducing the orthogonal complement of \mathcal{V}_0 and \mathcal{V}_1 as \mathcal{W}_0 , \mathcal{V}_1 can be written as

$$\mathcal{V}_1 = \mathcal{V}_0 \oplus \mathcal{W}_0, \quad (2.7)$$

where \oplus denotes the direct sum. Naturally via Equation (2.6) then L^2 may be represented as

$$L^2 = \mathcal{V}_0 \oplus \mathcal{W}_0 \oplus \mathcal{W}_1 \oplus \mathcal{W}_2 \oplus \dots. \quad (2.8)$$

The spaces \mathcal{W}_j are called the detail spaces. The vector spaces \mathcal{V}_0 and \mathcal{W}_j are spanned by a set of functions known as scaling functions and wavelet functions, respectively. Wavelets on finer scales may be defined by translations and dilations of the mother wavelet. Then any arbitrary function $f \in L^2$ may be expressed as linear combinations of the scaling functions and wavelets, with the coefficients of the wavelet functions being indicative of local features. These coefficients are called the detail coefficients.

With respect to the application of MR analysis to the solution of partial differential equations, the purpose of the Equation (2.8) is to represent the discrete solution on the finest level as a sum of the discrete solution values on the coarsest level plus a series of differences between adjacent levels. Then the detail coefficients of low magnitude indicate where solution features may necessitate less mesh resolution.

In practice, the wavelet functions are never actually constructed, and detail coefficients are obtained using a transform. The detail coefficients are thresholded according to a user-defined tolerance. This results in a compressed solution and (usually significantly) fewer mesh cells. For more details on the implementation of the MR-based AMR used in this work, the reader is referred to the work of Gusto & Plewa [20].

2.3.3 Additional remarks

Some details of the present approach should be mentioned. Firstly, the scheme described in Equation (2.3) is implemented in a Fortran code called Proteus, a fork of the FLASH code [17] developed at the University of Chicago. Proteus uses the piecewise parabolic method (PPM) [12] to treat the hydrodynamics, a thirteen isotope nuclear network [17] to solve the nuclear reactions,

and the Helmholtz equation of state (EoS) [58] to describe the thermodynamic state and close the governing system of equations. The parallel, block-structured adaptive mesh refinement routines are provided by the PARAMESH library [37].

Then the treatment of turbulence should be discussed. Due to the very low viscosity of the dense plasma, the Kolmogorov length scale [31] is quite small, on the order of centimeters. For the uninitiated reader, this value describes the scale on which the dissipation of turbulent kinetic energy becomes important. This is important, as the cutoff of grid resolution above this scale disrupts the energy cascade. As discussed, to include such scales in the full-star models is infeasible. Then practitioners generally resort to a large-eddy simulation (LES) approach [34], where the governing equations are filtered at some cutoff length, and a SGS model for describing the stresses on the unresolved scales is implemented. The filtered equations may also be solved *without* an explicit SGS model, but with some dissipation provided by numerically by the hydrodynamics solver. In the latter approach, known as implicit LES (ILES), it is hoped that the amount of numerical dissipation provides an *effective* viscosity similar to the viscosity of the actual turbulence. In [4], Aspden et al. actually quantify the effect that numerical dissipation has on the small scales using dimensional analysis.

The present modeling approach makes no use of any type of SGS model for the flame or for turbulence. The flame is simply propagated cell-to-cell via diffusion. These assumptions are mentioned to highlight the limitations of the present work.

CHAPTER 3

DIRECT NUMERICAL SIMULATION OF THE DEFLAGRATION-TO-DETONATION TRANSITION

3.1 Introduction

A substantial amount of evidence in the literature suggests that the Zel'dovich reactivity gradient mechanism may lead to spontaneous detonation initiation within small regions of relatively low induction times known as hotspots. The hotspots may form from the mixing of warm ash and cold fuel that occurs either when a flame front is broken via turbulence, or when a flame is quenched, as described by Khokhlov, Oran, & Wheeler [28]. Again, these authors consider two critical questions: (1) what conditions allow a detonation to form within a hotspot, and (2) what are the large-scale turbulence driving conditions that lead to such situations? Combined, the answers to these questions may help form the basis of a SGS model for DDT in simulations of exploding WDs. This chapter deals primarily with the former of these questions.

The study of Khokhlov et al. is limited by the small number of hotspot configurations considered and the size of the parameter space (i.e. imposing idealized conditions). How more physically-motivated profiles in induction time can alter the potential for detonation initiation was considered by Seitzzahl et al. [52]. However the addition of velocity fields and realistic initial conditions has not been addressed in the literature.

In this chapter the aforementioned works are expanded upon by using DNS to study a broader, physically motivated set of hotspot configurations likely to occur in the distributed burning regime. The chapter provides insight into how the criteria for detonation initiation may change when more realistic initial hotspot configurations are considered, and when realistic velocity fields are incorporated.

3.2 Methods

As discussed in Section 1.2.1, the theory proposed by Zel'dovich posits that a region with nonuniform induction time can produce a detonation if and only if the reactive wave can couple to the outgoing compressive wave. The compressive wave is produced once electron degeneracy

is lifted and burning can then result in an increase in thermal pressure within the nonuniformly preconditioned region.

The potential for the reactive wave to couple to the outgoing compressive wave is mainly determined by the spontaneous propagation velocity field u_{sp} , energy generation rates, and the soundspeed of the matter. Given that u_{sp} is the inverse of the spatial gradient of induction time, the initial spatial profile of the hotspot is critically important, although the profile can be expected to change considerably during the evolution due to feedback between reactive and hydrodynamic processes. Despite this, however, it is safe to say that for realistic profiles, the larger the radius is, the more mild the gradient in induction time will be, and the more likely the reactive wave will be able to catch up to the outgoing acoustic wave.

In the first series of investigations, the dependence of the successful detonation on the spontaneous propagation velocity is explored by modulating the spatial characteristics of a Gaussian initial profile. The dependence on the ambient density and temperature is also investigated. Besides partially determining the induction time, the density also controls to some extent the energy generation rates once the fuel is ignited. Given that the successful detonation depends on the feedback from the energy generation behind the compressive wave, the density can be expected to dramatically influence the process.

In the second series of investigations, a similar analysis is performed but with the initial conditions being drawn from realistic, three-dimensional turbulence simulations using one-dimensional extractions (lineouts).

3.2.1 Idealized initial conditions

Here the solution of Equation (2.2a)-Equation (2.2d) is obtained using DNS, with initial conditions being idealized hotspot profiles. The initial profiles are Gaussian, with the amplitude and variation of the profiles being free parameters. The ambient density and temperature are also free parameters in the present study. These greatly affect the magnitude of the induction time and the rate of energy release due to burning. The choice of a Gaussian function is made based on the findings in Appendix A, which indicate that the spatial profiles of fluctuations in the turbulent medium are fit by a Gaussian function to a high degree of accuracy.

In these models, referred to as *synthetic* models, an effort is made to try to isolate the spontaneous combustion mechanism to the greatest extent possible. To this end, a pressure gradient

of zero is prescribed in the whole domain, as well as zero velocity. This ensures that a successful detonation can only be triggered by coupling to a spontaneous, self-generated wave.

For every hotspot configuration the initial density profile is defined as

$$\rho(t = 0, x) := \rho_{\text{amb}} - \delta\rho \exp\left(\frac{-x^2}{2R^2}\right), \quad (3.1)$$

where ρ_{amb} is the ambient density value, $\delta\rho$ is the perturbation in density and R determines the radius of the perturbation. For notational convenience the normalized amplitude is introduced as $A = \delta\rho/\rho_{\text{amb}}$. The ambient pressure is obtained using the equation of state (EoS) with the desired ambient density and temperature as inputs. Then the density is perturbed according to Equation (3.1) and passed to the EoS routine again with the previously computed pressure to get the temperature profile. This process produces the desired Gaussian form in density, temperature, and induction time while also maintaining baroclinic (constant pressure) conditions.

A range of each of the aforementioned free parameters is chosen to build a database of models for analysis. The range of each of the free parameters chosen for inclusion in the database is informed by the statistics of 3D reactive turbulence studies introduced in Appendix A. In particular the largest normalized amplitude of the density perturbations in the reactive turbulent flow reaches roughly $A = 0.3$, while the radii of the perturbations reach about 1×10^5 cm. In the present database, the ambient density varies from 7.5×10^6 g cm⁻³ to 3×10^7 g cm⁻³, and the ambient temperature varies from 1.55×10^9 K to 2.2×10^9 K. The fuel concentration is kept constant at a mix of 50/50 C/O. Naturally, the fuel concentration may also be varied. In the present study however, it is fixed in order to keep the parameter space manageable. Sampling within the chosen parameter ranges is done adaptively, with a base grid of equispaced samples computed initially, and additional samples generated using a bisection approach to locate the region of discontinuity.

The computational setup considers the solution of Equation (2.2a)-Equation (2.2d), with the hotspot centered in the domain with $x \in [-1.2 \times 10^5, 1.2 \times 10^5]$ cm, and with outflow conditions prescribed at each boundary. The simulation is run until either $t = 4.0 \times 10^{-4}$ s or a detonation is formed. The timestep is determined dynamically via the CFL condition [13] or the nuclear burning timescale depending on which is smaller. The maximum resolution in these models is $\Delta x \approx 19.53$ cm, ensuring that spatial structures such as shocks are very well resolved. Multiresolution

mesh adaptation is used to ensure that sharp structures are resolved without wasting resources in inactive areas of the domain¹.

In order to determine the outcome of each model, the maximum Mach number is used as an indicator. In models with detonation-forming hotspots the maximum Mach number reaches or exceeds one. This value is reported by the simulation code at every timestep. This offers a simple way to classify the results.

3.2.2 Realistic initial conditions

Hotspots that are not synthetically formulated but rather sampled from realistic turbulent conditions are considered. In these models, referred to as *turbulence extracted* models, data is extracted directly from three-dimensional reactive turbulence simulations (as described in Section 2.2.3) to create the initial conditions.

The dynamics are much the same from the point of view of the Zel'dovich mechanism. In other words the system can still be described as a competition between energy release on one hand and acoustic energy propagation on the other. However the extent to which the process is influenced by turbulent motions remains to be seen. Aside from arbitrarily complex velocity fields, the effect of nontrivial initial profiles (i.e. not of a simple Gaussian or polynomial form) is also of interest.

The extraction of hotspot profiles from the 3D turbulence data follows several steps, outlined below:

1. one-dimensional sweeps through the principal axes (x, y, z) of the 3D data are made;
2. hotspots are identified within the one-dimensional sweep by analyzing fluctuations in temperature or density;
3. a window of data is extracted with the hotspot centered within it;
4. interpolation of the density, temperature, velocity, and carbon abundance is performed within the window;
5. the interpolated profiles are resampled at the new resolution and may be used as initial conditions for DNS calculations.

Once this procedure is complete the interpolated profiles may be used as-is, or they may be modified. In the present study these profiles are modified by increasing slightly the temperature everywhere

¹In these studies the refinement tolerance is very strict. Virtually every region with nonzero velocity is refined to the maximum level. Still, there are substantial computational savings given that the hotspot takes up a small portion of the domain initially.

equally, bringing each model closer to ignition. To perform interpolation, the piecewise cubic hermite interpolating polynomial (PCHIP) implementation in Matlab is used.

The computational setup for these models is nearly identical to the synthetic models. Here though the domain is increased, with $x \in [-2 \times 10^5, 2 \times 10^5]$ cm, and the grid resolution consequently being increased slightly to $\Delta x \approx 24.41$ cm.

Although the conditions for these models are extracted from forced turbulence simulations described in Chapter 2, forcing is not applied in these models once they are begun. The relevant timescale for a detonation-developing hotspot is less than the characteristic timescales of the turbulence considered in this work. These timescales are on the order of 10^{-2} cm; this is over one order of magnitude larger than the timescale of interest. Then the injection of momentum on those timescales cannot be expected to play a significant role during the evolution and is consequently neglected.

The pre-existing velocity field in these models introduces a few complications when it comes to labeling of the large dataset. Because there are some model configurations with strong non-zero mean velocities, the Mach number cannot be used as a reliable indicator of detonation. Instead a filtering function is introduced that analyzes jumps in pressure, temperature, density, and velocity across the wave. This filtering function is a core part of the automatic labeler used to correctly determine the outcomes of such a large database of simulations.

In the automatic labeler, a sample is declared to produce a detonation if the jumps found in the vicinity of the original hotspot satisfy certain criteria for detonations. Given state 1 ahead of the wave and state 2 behind it, a detonation is defined as having conditions in pressure of $p_2/p_1 > 2$, in temperature of $T_2/T_1 > 2$, in density of $\rho_2/\rho_1 > 2$, and in relative velocity of $|u_2 - u_1|/u_1 > 0.6$. It is also required that the carbon abundance is reduced across the wave such that $X_{f,2}/X_{f,1} < 0.1$. These conditions are determined empirically.

To account for advection of the hotspot in a strong mean velocity field, a spatially adaptive monitoring window is used that evolves with the hotspot in time based on the magnitude of the mean velocity. A time limit for the hotspot to undergo detonation is imposed; it is defined as three quarters of the minimum induction time value plus one sound-crossing time. If a detonation is not detected within this time then the sample is declared as non-detonation-forming.

Some additional logic must be applied to the automatic labeler for certain problematic cases. One such case occurs when divergence of the velocity field causes fluid to build up in another part of the domain. This fluid can be preconditioned such that a new rapidly burning hotspot is formed

outside of the monitoring window. If the hotspot then successfully detonates, the detonation wave may enter the monitoring region centered around the original hotspot and trigger a false positive for that sample. To avoid this when analyze the characteristics of the detected detonation wave - if it is to the right of the hotspot center and the wave is moving to the left (or vice versa), then it could not have been generated by the hotspot of interest and the samples is removed.

3.2.3 Analysis approach

In the present analysis, the potential for detonation initiation within each hotspot configuration is measured according to Equation (2.1). In particular the sound-crossing timescale and the reactive timescale are computed for each sample. It is expected that for a fixed reactive timescale, a critical value in sound-crossing time can be identified such that no detonation can occur for values smaller than the critical value.

To measure the reactive timescale at the initial state, the reactive time scale is computed as σ_0 , the standard deviation of induction times within some region r_0 . The sound-crossing time is computed as $r_0/\langle c_0 \rangle$, where $\langle c_0 \rangle$ is the mean soundspeed in the region.

There is some freedom in choosing the size of the sampling region r_0 . The goal in choosing this region is to include all of the material reacting on timescales on the order of the smallest timescale. For a hotspot whose induction time minimum is located at $x = 0$, the radius for the side with $x > 0$ is defined as

$$r_0 = \arg \min_{x>0} \left| \frac{\tau(x) - \min \tau}{\min \tau} - \varepsilon \right|, \quad (3.2)$$

where ε is some threshold². In other words, the boundary of the region is defined by a relative drop in induction time from the minimum point. In testing it has been found that the choice of ε does not have much effect on the establishment of a critical value in the evaluation of Equation (2.1). Based on numerical experiments, a value of $\varepsilon = 1.4$ is found to be a sensible choice.

For the symmetric synthetic models, the analysis is applied to the half-profiles. However for the non-symmetric TE models, the analysis is applied to both sides of the hotspot independently, with the center of the hotspot being defined as the point of lowest induction time.

3.3 Results

In this section the results of a total of 27, 791 hotspot configurations are presented, with 2, 522 being synthetic configurations and 25, 269 being extracted from turbulence. In Table 3.1 a summary

²Naturally, for the side with $x < 0$, $\arg \min_{x<0}$ is used in Equation (3.2).

Name	ρ_{amb}	T_{amb}	A	R	Runs
GLtHt	0.75×10^7	1.78×10^9	0.04 – 0.32	$2 \times 10^3 - 3 \times 10^4$	138
GMdCd	1.0×10^7	1.66×10^9	0.02 – 0.3	0.02 – 0.3	400
GMdWm	1.0×10^7	1.72×10^9	0.02 – 0.3	0.02 – 0.3	274
GMdHt	1.0×10^7	1.78×10^9	0.005 – 0.2	0.02 – 0.2	1480
GHvHt	1.33×10^7	1.78×10^9	0.04 – 0.2	$2 \times 10^3 - 2 \times 10^4$	95
GRND	$1 \times 10^7 - 3 \times 10^7$	$1.55 \times 10^9 - 2.2 \times 10^9$	0.02 – 0.3	$0.2 \times 10^4 - 4 \times 10^4$	135
TE	$0.91 \times 10^7 - 1.04 \times 10^7$	$1.18 \times 10^9 - 2.04 \times 10^9$	-	-	25269

Table 3.1: Description of databases showing the range of ambient density and temperature for each database as well as the normalized amplitude and width (for Gaussian models). The total number of configurations is shown for each database.

of the executions is presented. The synthetic models are divided into several smaller databases based on the ambient density or temperature. Overall, three temperatures are tested for the synthetic models: $T_{\text{amb}} = 1.66 \times 10^9$ K, $T_{\text{amb}} = 1.72 \times 10^9$ K, and $T_{\text{amb}} = 1.78 \times 10^9$ K. These are labeled as cold (**Cd**), warm (**Wm**), and hot (**Ht**). The density at the hottest temperature is also varied, using values of $\rho_{\text{amb}} = 0.75 \times 10^7$ g cm⁻³, $\rho_{\text{amb}} = 1 \times 10^7$ g cm⁻³, $\rho_{\text{amb}} = 1.33 \times 10^7$ g cm⁻³, while for the other two temperatures the density is held at $\rho_{\text{amb}} = 1 \times 10^7$ g cm⁻³. These densities are labeled as light (**Lt**), medium (**Md**), and heavy (**Hv**). Synthetic models and turbulence-extracted models are differentiated by appending the codes of synthetic databases with a **G** for Gauss. Finally the database codes are combined in order of the model type, density, temperature.

An additional dataset, **GRND**, is executed with the four free parameters being sampled randomly and nonuniformly over slightly larger intervals as summarized in the table.

Finally, note that when referring to a specific model the additional two free parameters, amplitude and radius, are included. The normalized amplitude is denoted by **A** followed by two digits, and the radius is denoted by **R** with three digits following. For example, model **GMdHtA05R110** is a synthetic model with an ambient density of $\rho_{\text{amb}} = 1 \times 10^7$ g cm⁻³, ambient temperature of $T_{\text{amb}} = 1.78 \times 10^9$ K, an normalized amplitude of $A = 0.08$, and a radius determined by $R = 1.1 \times 10^5$ cm.

For the **TE** models a similar code is used for naming. The code begins with **TE** followed by the approximate ambient temperature, abbreviated **ta**, and its value, then the maximum temperature, **ta**, and its value, then the approximate radius, **rd**, and its value. For instance a **TE** model with an approximate ambient temperature of $T_{\text{amb}} = 1.72 \times 10^9$ K, a maximum tempera-

ture of $T = 2.12 \times 10^9$ K, and an approximate radius of $R = 4.5 \times 10^4$ cm would be denoted as TEta17200tm21200rd00450.

3.3.1 Idealized initial conditions

Idealized initial conditions are used to explore the basic conditions necessary for a detonation to develop from a hotspot via the Zel’dovich mechanism. First, two models that are adjacent in the parameter space are investigated. In the first model, GMdHtA08R130, the normalized amplitude of the perturbation is $A = 0.08$ and the variation is $R = 1.3 \times 10^4$ cm. In Figure 3.1 the evolution of

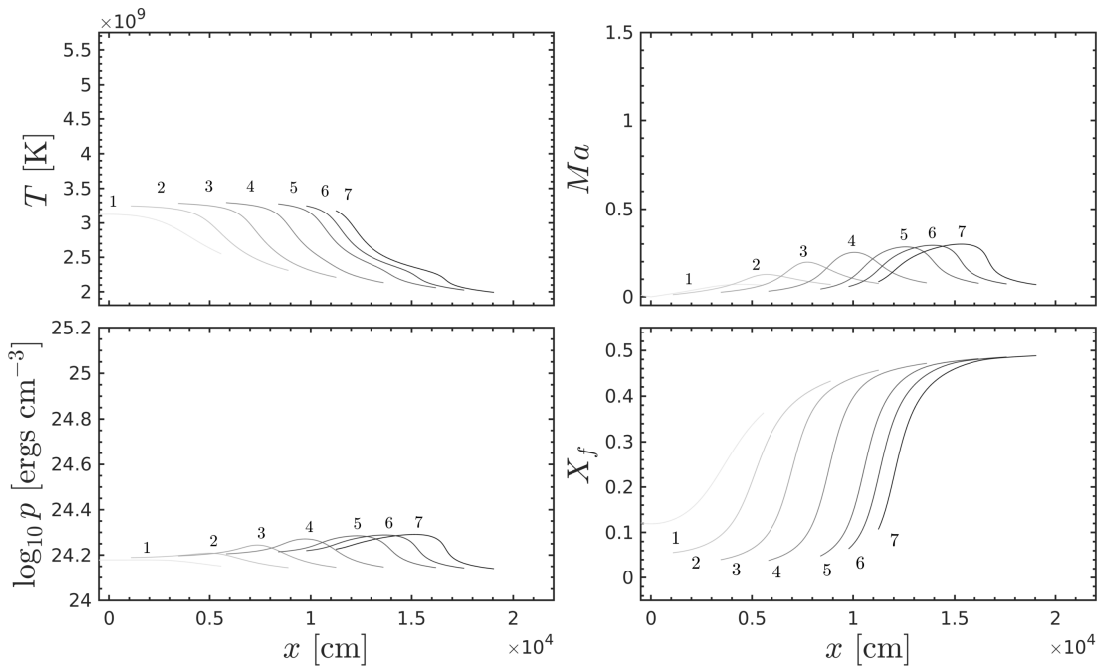


Figure 3.1: Evolution of a synthetic hotspot, model GMdHtA08R130, with $A = 0.08$ and $R = 1.3 \times 10^4$ cm that results in a deflagration. Numerals 1 through 7 in the annotations refer to times $t_1 = 1.6$ ms, $t_2 = 1.65$ ms, $t_3 = 1.7$ ms, $t_4 = 1.75$ ms, $t_5 = 1.8$ ms, $t_6 = 1.825$ ms, and $t_7 = 1.85$ ms, respectively. Highlighted portions of the temperature, Mach number, pressure, and carbon abundance are shown at each time.

temperature, Mach number, pressure, and carbon abundance is shown at seven instances in time, namely at $t_1 = 1.6$ ms, $t_2 = 1.65$ ms, $t_3 = 1.7$ ms, $t_4 = 1.75$ ms, $t_5 = 1.8$ ms, $t_6 = 1.825$ ms, and $t_7 = 1.85$ ms.

In profile 1 temperature is observed reaching its maximum of around 3.15×10^9 K, the Mach number reaching a maximum of about 0.1, pressure still roughly constant near its original isobaric

state, and the carbon abundance in the central region at about 0.12. From this point in time the system progresses rapidly. By t_2 the pressure has developed a definitive peak as the divergence in velocity due to the expanding gas has caused material to pile up. At this stage the carbon abundance profile (lower right panel) indicates that the width of the reaction zone has decreased substantially. In profiles 3 and 4 the trend of pressure buildup and reaction zone steepening continues at a similar pace. From t_4 to t_5 however it is observed that the increase in pressure begins to stall. Between t_5 and t_6 , again, only a mild acceleration of the gas occurs. By t_7 it is evident that the process has failed to accelerate any further.

This model exemplifies the situation where only a deflagration, not a detonation, is produced. While a clear coupling between the reactive and compressive waves is initially observed, resulting in an increase of pressure and steepness, this coupling becomes less efficient as the wave moves down the temperature gradient into colder, denser fuel. Then pressure wave can no longer provide the amount of compression needed to precondition the reaction zone behind it. The consequence is that the energy release behind the wave is no longer able to drive the pressure wave, resulting in the acceleration process stalling completely.

The previous failed detonation scenario is contrasted with that of model GmDhtA08R140. This model starts with nearly identical initial conditions, except that the radius of the initial perturbation is slightly greater. In Figure 3.2 the evolution of the same four quantities is shown on the same scales. Profiles are drawn at the same times as in the previous case. Profile 1 shows the initially burned material with a maximum temperature of around 3.2×10^9 K, and a carbon fraction of about 0.095. As in the case of model GmDhtA08R130, it is observed that by t_2 a definitive peak in pressure has developed. Again, a steady rise in pressure is observed between t_2 and t_4 . The difference in outcomes between the two models becomes evident by t_5 , where one can clearly observe a steepening of the pressure wave. From this point in time the feedback process appears to occur rapidly. A sharp rise in temperature behind the compressive wave is visible in profile 6, as is the steepening of the carbon abundance. Profile 7 shows a Mach number above 1 (supersonic fluid velocity) as well as the nearly complete exhaustion of fuel behind the detonation wave.

The intuition that a wider initial profile with more mild gradients of the induction time should lead to more favorable conditions for a detonation is proven correct in this case. It can be seen that the conditions upstream of the compressive wave vary more gradually than in the prior case, reducing the rate at which material must be compressed in order to feed the reaction zone with preconditioned fuel.

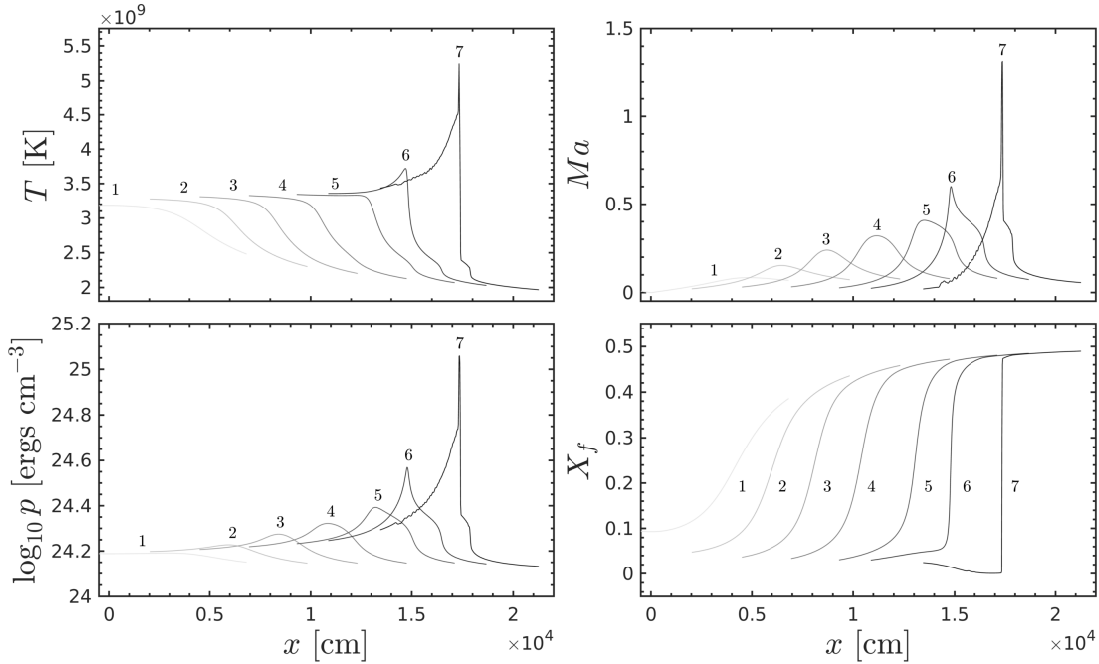


Figure 3.2: Evolution of a synthetic hotspot, model GMdHtA08R140, with $A = 0.08$ and $R = 1.4 \times 10^4$ cm that results in a detonation. Numerals 1 through 7 in the annotations refer to times $t_1 = 1.6$ ms, $t_2 = 1.65$ ms, $t_3 = 1.7$ ms, $t_4 = 1.75$ ms, $t_5 = 1.8$ ms, $t_6 = 1.825$ ms, and $t_7 = 1.85$ ms, respectively. Highlighted portions of the temperature, Mach number, pressure, and carbon abundance are shown at each time.

In Figure 3.3 the space-time curves of the outgoing compressive and reactive waves are plotted for models GMdHtA08R130 (top panel) and GMdHtA08R140 (bottom panel). The position of the compressive wave is determined by the location of the peak in pressure of the outgoing wave and the position of the reactive wave is computed as the first point behind the wave reaching less than one half of the ambient fuel abundance, X_f .

In both cases the speed of the compressive and reactive waves is initially high (roughly before t_1). The compressive wave slows down when it begins to encounter colder and more dense upstream fuel near t_1 . Between t_1 and t_2 the compressive wave builds strength, driven by the initial overpressure within the central region of the hotspot. Eventually, the peak of the compressive wave overtakes the reactive wave (near t_2). From this point there is a chance for the feedback mechanism to take hold. In the case of GMdHtA08R130, the reactive wave falls behind due to inefficient preconditioning of the upstream fuel by the compressive wave. In the case of GMdHtA08R140 it is observed that the feedback process is more efficient, and although the waves diverge from t_2 to t_3 , somewhere

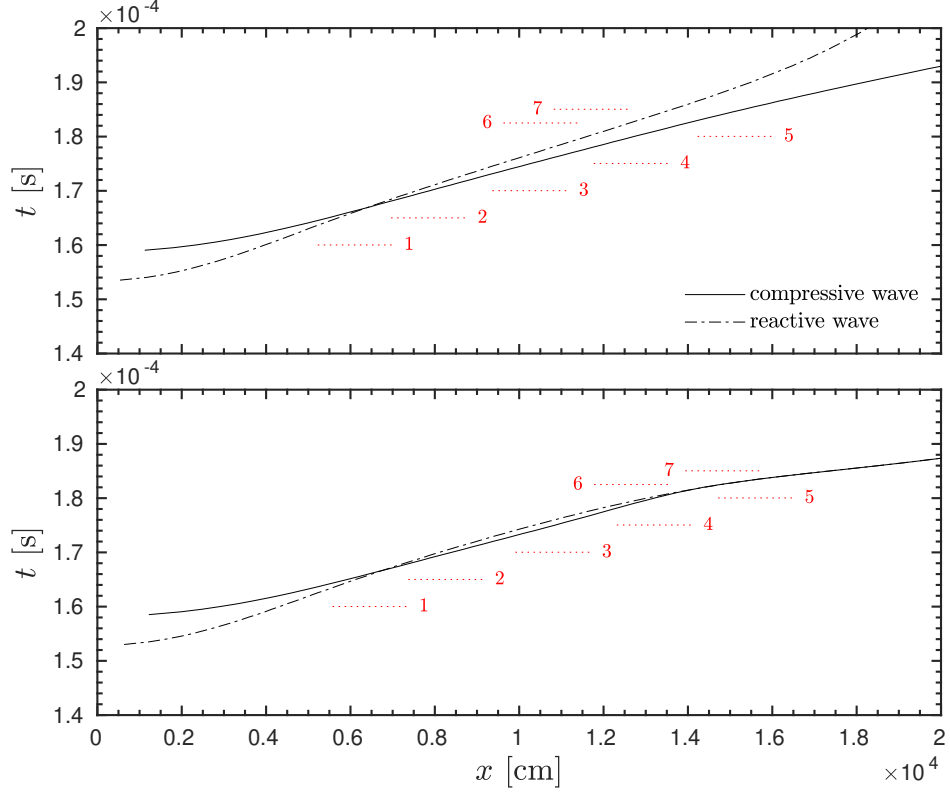


Figure 3.3: Space-time diagrams of the compressive and reactive waves in both a non-detonation-forming case (top; model `GMdHtA08R130`) and a detonation-forming case (bottom; model `GMdHtA08R140`). The times t_1 through t_7 are labeled in red for added context.

between t_3 and t_4 this trend is reversed and the reactive wave accelerates. By t_6 the two waves become completely coupled and the velocity of the combined shock-reaction complex accelerates significantly.

These two cases effectively illustrate the role of the spatial characteristics of the hotspot in determining its viability for detonation initiation. Then the dependence of the ability of the hotspot to form a detonation as a function of amplitude, A , and width, R is examined. In Figure 3.4 a phase diagram is shown that separates the simulation outcomes from dataset `GMdHt` into three regions: volumetric burning, carbon deflagration, and carbon detonation. In the volumetric burning regime, no significant acoustic wave is generated because the amplitude is so small that no significant amount of energy is released through nuclear burning. The threshold for volumetric burning is defined as $Ma < 0.01$. In the deflagration regime, a significant amount of energy is released through burning, however the coupling process does not occur. Still, the process may produce a strong outgoing shockwave and flame behind it. Finally, in the third regime, a detonation wave is

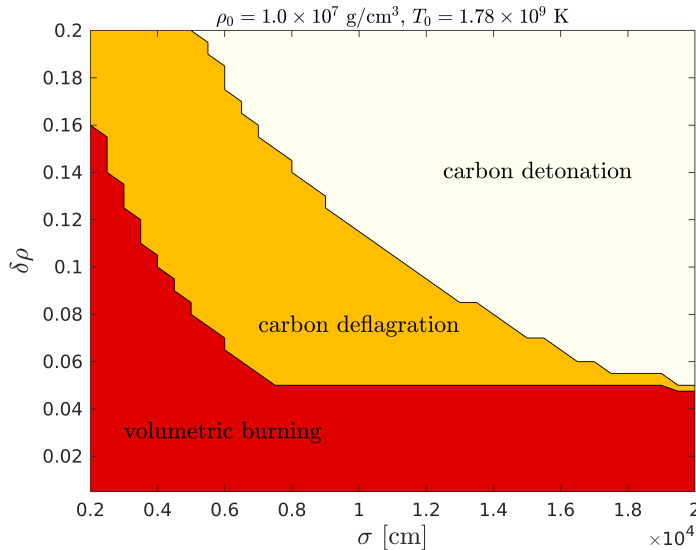


Figure 3.4: Phase diagram illustrating the dependence of the ability of a hotspot to form a detonation as a function of amplitude and width, at a fixed ambient density and temperature of $\rho_{\text{amb}} = 1 \times 10^7 \text{ g cm}^{-3}$ and $T_{\text{amb}} = 1.78 \times 10^9 \text{ K}$ (dataset GMdHt) respectively. Three regions are identified: volumetric burning, carbon deflagration, and carbon detonation.

created due to successful coupling between the reactive and compressive waves.

Next the entire dataset is analyzed and the characteristics leading to detonation are quantified more precisely. The timescale analysis of Khokhlov is applied using Equation (2.1) with the criteria introduced in Equation (3.2) to define the ‘width’ of the region (as some additional specificity is required).

Figure 3.5 is a novel result that shows the critical values on the reactive versus sound-crossing timescale plot (in log scale) for various combinations of ambient density and temperature. Each curve divides the regions of non-detonation-forming and detonation-forming conditions for the corresponding dataset.

According to Equation (2.1), a detonation is only possible when the reactive timescale, given by the variation in induction times σ_0 , is approximately smaller than the sound-crossing timescale, given by $r_0/\langle c_0 \rangle$. It is observed that for the three datasets at the intermediate ambient density of $\rho_0 = 1 \times 10^7 \text{ g cm}^{-3}$, GMdCd (dashed line), GMdWm (dotted line), and GMdHt (dash-dotted line), the critical values are closely aligned. For the datasets with varying ambient density, GLtHt (thin solid line) and GHvHt (thick solid line), a shift in the plane is observed. In particular for the dataset with higher density a shift of the critical values toward smaller sound-crossing times is observed, and

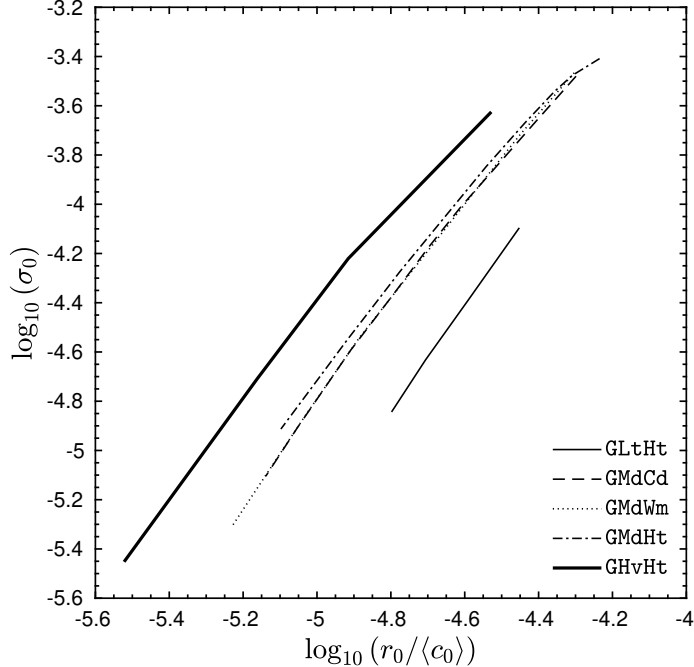


Figure 3.5: Critical conditions for DDT obtained by DNS of synthetically generated hotspot configurations. Shown are the contour lines separating the non-detonation-forming and detonation-forming regions of the reactive versus sound-crossing timescale plane for five databases of varying ambient density and temperature.

for the dataset with lower density the opposite is observed. In other words, for hotspots at higher densities these results indicate that the the sound-crossing time does not need to be as large in order for a detonation to occur, while for hotspots at lower densities the opposite is true. Or put another way, for a given sound-crossing timescale, hotspots with higher densities require a smaller degree of synchronization of burning induction times (larger σ_0) to achieve coupling between the reactive and compressive waves.

Given that the soundspeed is not very sensitive to density (being proportional to the inverse of the square root of density), these results do indeed seem to indicate that smaller regions (r_0) are sufficient for the hotspot to form a detonation in the case of dataset **GHvHt**. This can be attributed to the heat capacity of the material being lowered with increasing density, meaning that higher temperatures and possibly higher rates of energy generation can be reached during the spontaneous combustion process when compared to the models at the intermediate density.

Again, the inverse appears to be true in the lower density case. Compared to the high and intermediate densities a much larger sound-crossing time (i.e. a larger region) is required for a detonation to occur. For a given $\log_{10}(\sigma_0)$ value (for example -4.85), it is observed that the

minimum sound-crossing time required for detonation increases in intervals of about 0.2 in log-scale across the three models. These results corroborate the results in Figure 2.2. They have implications for the possibility of DDT in a delayed detonation scenario.

Here the possible limitations of this analysis is disclosed. First, it is clear that the sound-crossing time cannot extend indefinitely while the hotspot remains intact. In a turbulent flow, the hotspot will be destroyed by turbulence within the amount of time it takes eddies on a similar spatial scale to turn over. This natural condition is emulated in the present studies by the time limit imposed in the simulation. Its effect can be observed toward the upper right region of Figure 3.5, in which the curve corresponding to database `GMdHt` curves sharply to the right.

Secondly, there is also a theoretical limit on the extent of the reactive timescale. As σ_0 goes toward zero, the initial explosion takes place faster and faster, and in the limit, the case of the constant-volume explosion is reached. The critical size of the region cannot scale accordingly because of the physical constraint of thermal conductivity; as the size of the region becomes extremely small the reactions become thermally coupled due to thermal conduction [27]. In this scenario no spontaneous propagation is possible.

Finally the same analysis is applied to the dataset `GRND`. This dataset samples randomly in the space of ambient density, ambient temperature, normalized amplitude, and width corresponding to the ranges presented in Table 3.1. Due to the large degree of variation in the ambient density, a clear distinction between detonation-forming and non-detonation-forming models in the reactive versus sound-crossing timescale plane is not observed.

3.3.2 Realistic initial conditions

The same analysis approach is applied to the DNS studies of hotspot configurations with realistic initial conditions in the `TE` database. In Figure 3.6 the evolution of model `TEta17159tm21591rd00344` is shown for the temperature, Mach number, pressure, and carbon abundance. Relevant portions of the profiles are shown at times $t_1 = 60.1$ ms, $t_2 = 110.1$ ms, $t_3 = 120.1$ ms, $t_4 = 130.1$ ms, $t_5 = 140.1$ ms, $t_6 = 150.1$ ms, and $t_7 = 160$ ms.

The evolution proceeds similarly to the cases in the Gaussian datasets. Here however it is first observed that even at t_1 there is already a strong velocity field in the positive x direction, with a Mach number of around $Ma = 0.075$. From this point in time, rapid burning in the center of the hotspot is observed (already the center has been advected away from $x \approx 0$ to $x \approx 0.4$) between t_1 and t_3 followed by an increase in pressure within that region. Between t_3 and t_4 the pressure

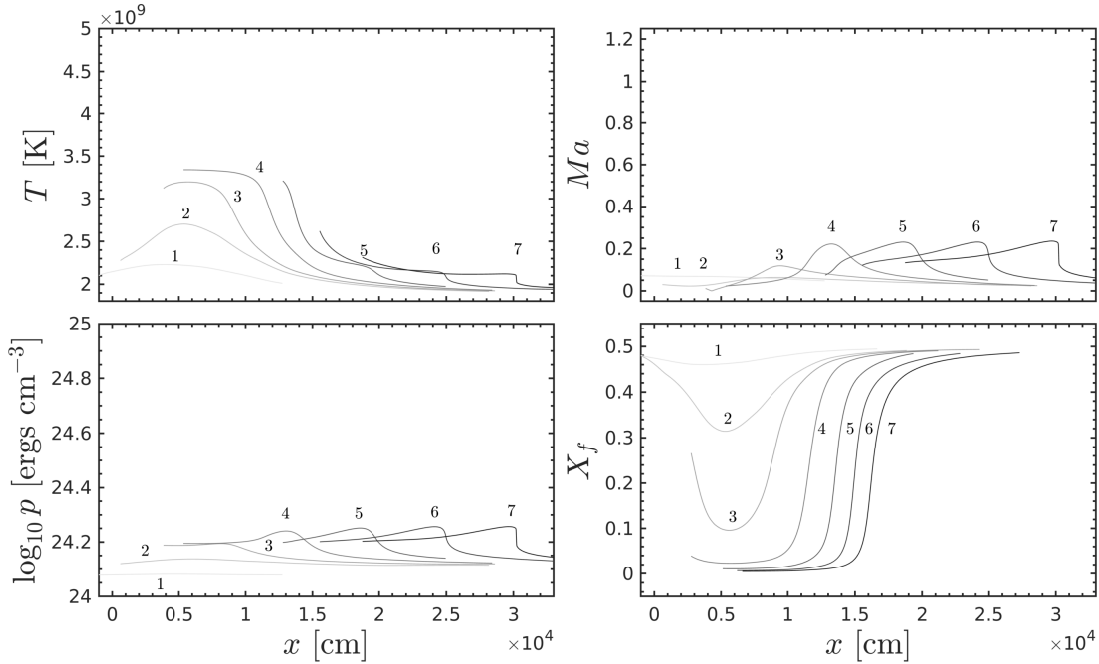


Figure 3.6: Evolution of a turbulence extracted hotspot, model T η a17159tm21591rd00344, that results in a detonation. Numerals 1 through 7 in the annotations refer to times $t_1 = 60.1$ ms, $t_2 = 110.1$ ms, $t_3 = 120.1$ ms, $t_4 = 130.1$ ms, $t_5 = 140.1$ ms, $t_6 = 150.1$ ms, and $t_7 = 160$ ms, respectively. Highlighted portions of the temperature, Mach number, pressure, and carbon abundance are shown at each time.

wave begins to steepen, forming a compressive wave that accelerates burning. The increase in burning may be observed in the near complete exhaustion of carbon behind the wave at t_4 (profile 4 in the bottom right panel near $x \approx 1 \times 10^4$). Between t_4 and t_5 however it becomes evident by comparing the position of the reaction zone and the compressive wave that the two have failed to couple. While the compressive wave continues to steepen after this point, the possibility of a coupled shock-reaction structure is impossible.

Next a case that successfully detonates is considered, model T η a16760tm21298rd00594. The evolution of this model is shown in Figure 3.7 at times $t_1 = 0$ ms, $t_2 = 120$ ms, $t_3 = 140$ ms, $t_4 = 150$ ms, and $t_5 = 160$ ms. Note that in this case the region of low induction times is wider than in the previous case. Additionally, note the absence of a significant velocity field, as evident in the first Mach number profile at t_1 .

It can be observed that between t_1 and t_3 a large region of material roughly 8×10^4 cm in

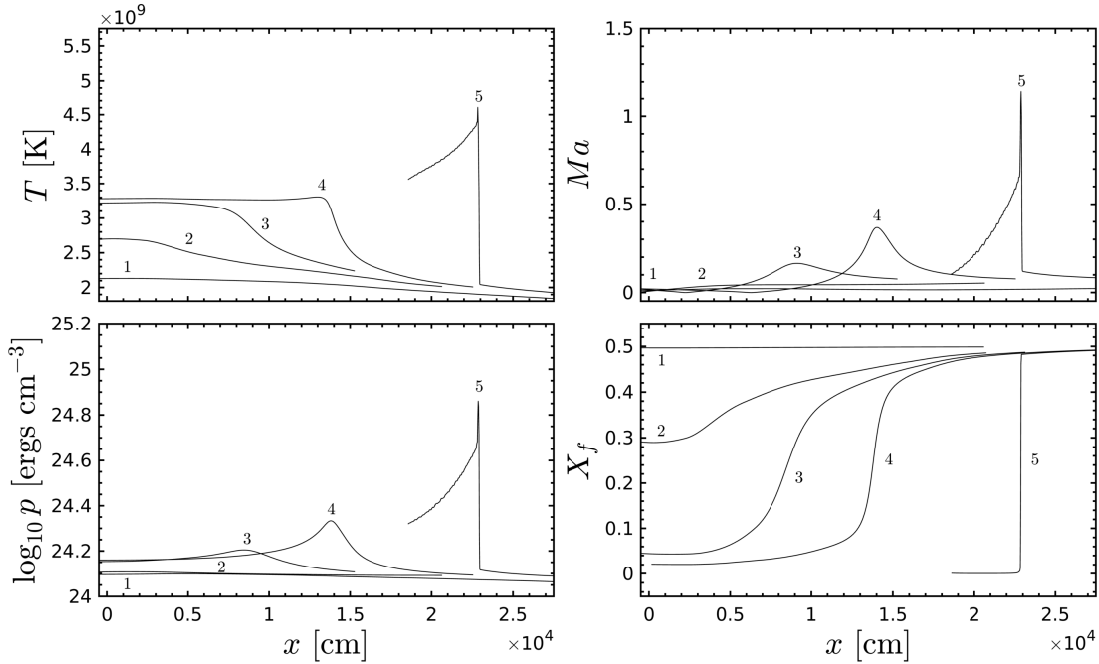


Figure 3.7: Evolution of a turbulence extracted hotspot, model `TEta16760tm21298rd00594`, that results in a detonation. Numerals 1 through 7 in the annotations refer to times $t_1 = 0$ ms, $t_2 = 120$ ms, $t_3 = 140$ ms, $t_4 = 150$ ms, and $t_5 = 160$ ms, respectively. Highlighted portions of the temperature, Mach number, pressure, and carbon abundance are shown at each time.

radius, undergoes complete burning, resulting in a pressure wave which can be seen in profile 3 in the bottom left panel. At this time, t_3 , the corresponding Mach number is roughly 0.2. The speed of the compressive wave dramatically increases between t_3 and t_4 , reaching a value of about 0.35. This feedback process continues to steepen the compressive wave and accelerate burning. By t_5 a fully fledged detonation wave emerges.

Considering now the analysis of the whole set of TE simulations, the previous analysis is applied, and the reactive and sound-crossing timescales are computed and plotted. The data is divided into non-detonation-forming and detonation-forming samples, and a bivariate histogram is computed for each. These results are shown in Figure 3.8 where it is observed that for the non-detonation-forming set (left panel), the vast majority of points, indicated by intensity of color, lie above and to the left of the curve of critical values found from the `GMdHt` dataset. This result is somewhat expected given that the density of models in the TE dataset fluctuates around 1×10^7 g cm $^{-3}$ by up to about fifteen percent (again, the ambient density in dataset `GMdHt` is fixed at 1×10^7 g cm $^{-3}$).

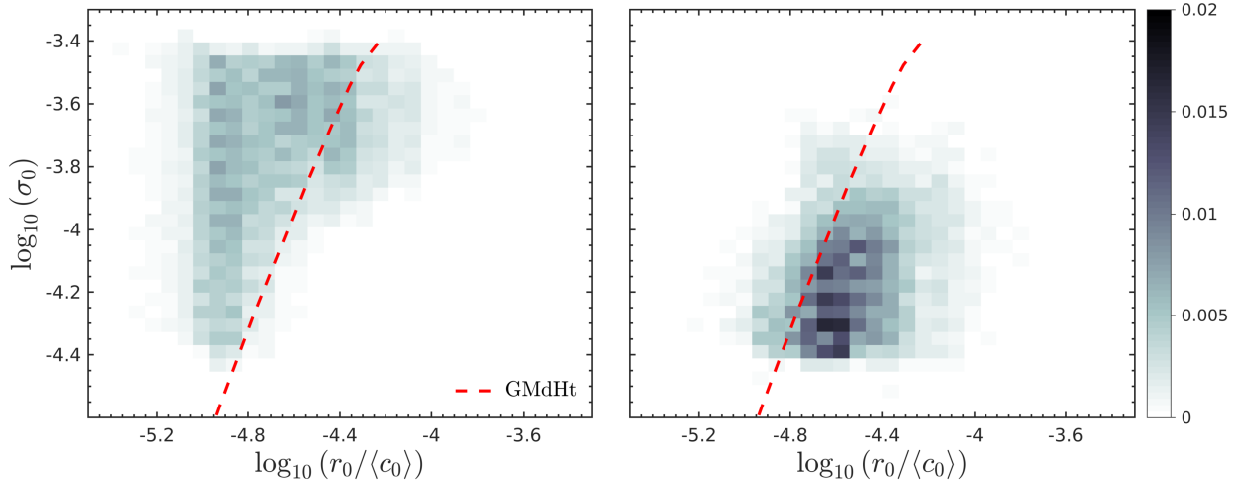


Figure 3.8: The TE dataset on the reactive versus sound-crossing timescale plane, separated into two panes with the left pane showing the bivariate histogram of non-detonation-forming points and the right pane showing the same but for the detonation-forming points. The colorscale indicates the probability of a point corresponding to that bin. Shown with a dotted red line is the contour from the GMdHt dataset for reference.

Many non-detonation-forming samples with higher overall timescales are seemingly located in the detonation-forming region of the plane. These models are the result of the conservative, early termination approach to labeling described in Section 3.2.2.

For the set of detonation-forming points (right panel) it is observed that the majority lie below and to the right of the reference curve, consistent with expectations. There is a set of detonation-forming points that lie across reference curve, however. It is possible that these cases may be explained by higher densities or a region of negative divergence of velocity in the region helping to compress the material in the potential detonation formation region.

3.4 Discussion

The new series of computational studies introduced in this chapter have been analyzed using the approach of Khokhlov, in particular by comparing the reactive and sound-crossing timescales. The results indicated that in trivially simple cases this analysis can distinguish between non-detonation-forming hotspots and detonation-forming hotspots. Of course, as observed in Figure 3.5, the critical conditions depend strongly on density (more so than on the ambient temperature). Additionally,

when non-trivial initial conditions are used, particularly when significant velocity fluctuations are present, additional analysis seems necessary to explain the exact cause of the deviations.

The obvious question raised by the results in Figure 3.8 is why the critical values of the reactive and sound-crossing timescales corresponding to samples from the TE dataset do not more closely align with the reference values. The first consideration is, as already stated, that the initial density in these models naturally fluctuates given that the conditions were extracted from turbulence with relative fluctuations of around 15%. This explains some deviation from the reference curve. For instance the detonation-forming points to the left of the reference curve may be toward the higher end of the density range, shifting the critical radius toward smaller values.

3.4.1 A critical radius for detonation

The determination of a critical radius for detonation, whose existence has been alluded to in several works [28, 45], is not trivial in realistic conditions. If such a thing as a critical radius can be meaningfully defined then it certainly is not independent of at least several other factors that influence the outcome of a reacting hotspot region, for example large-scale turbulent motions (in particular the divergence of velocity). Obviously the outcome is sensitive to the density of the matter as already observed, and probably also to the rates of nuclear energy generation, however this has not been explicitly tested (and indeed the findings of Khokhlov [27] suggest only a small dependence; see Figure 2.2).

It has been suggested in [45] that perhaps the most important criteria for detonation formation of hotspots is whether or not the reactive wave speed reaches the Chapman-Jouget velocity somewhere along the profile. In [27] the region where the reactive wave speed equals the sonic velocity is denoted by r_s , with some critical value r_s^* . Again however, the existence of such a value seems precarious because of the reasons just discussed. The reactive wave speed field is simply computed by the inverse of the gradient of induction time and contains basically no information about density, potentially adverse velocity or pressure gradients, or the nuclear energy generation rates.

In Figure 3.9 the dependence of the maximum Mach number achieved on the value r_s and the density across several values of relative amplitude, A , is presented. It is found that the cases with higher ambient density achieve detonation with a smaller value of r_s and vice versa. This finding is similar to the relationship observed between density and the critical sound-crossing time in Figure 3.5.

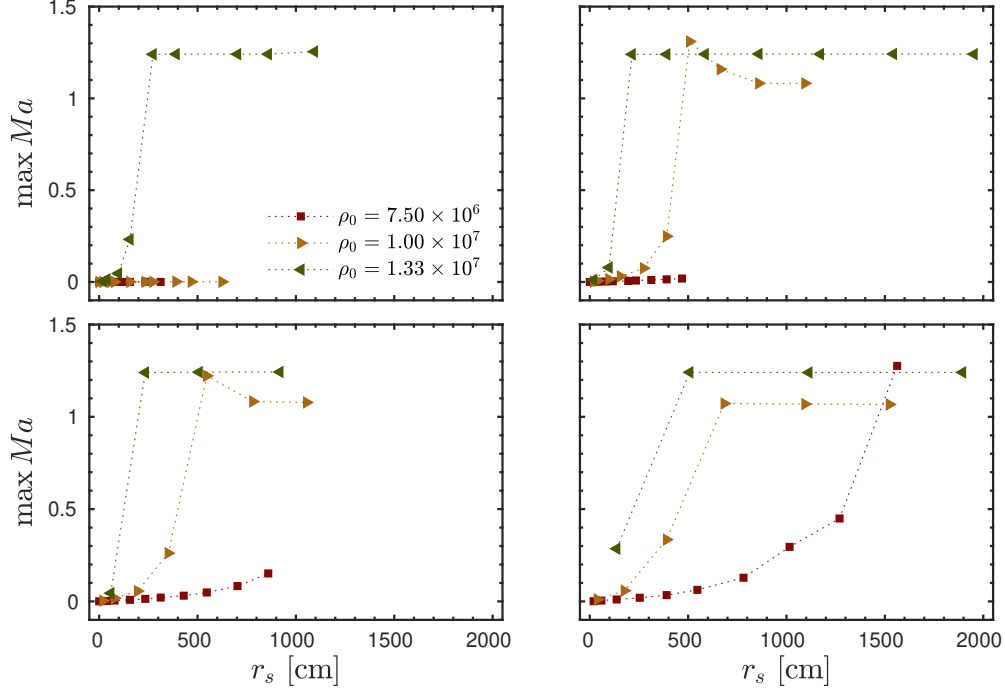


Figure 3.9: Comparison of maximum Mach number reached versus r_s for ambient densities of $\rho_{\text{amb}} = 7.5 \times 10^6 \text{ g cm}^{-3}$ (red squares), $\rho_{\text{amb}} = 1.0 \times 10^7 \text{ g cm}^{-3}$ (gold right-arrows), and $\rho_{\text{amb}} = 1.33 \times 10^7 \text{ g cm}^{-3}$ (green left-arrows), and for four normalized amplitudes: $A = 0.04$ (top left), $A = 0.08$ (top right), $A = 0.12$ (bottom left), and $A = 0.16$ (bottom right).

Overall the smallest value of r_s found to produce a detonation in the present synthetic studies suggests a critical value of about $r_s^* \approx 200 \text{ cm}$. If r_s is any smaller than this value then the formation of a detonation is impossible. However it is notable that these results are limited by the choice of parameters used to define the hotspot in the present study. Smaller values may be possible.

3.4.2 Concluding remarks

Overall, it seems that the semi-analytic characterization of hotspots using the approach of Khokhlov is useful, but it is not sufficient for determining the outcome of hotspots with a high degree of accuracy, especially when the other factors mentioned earlier in the chapter are considered. The present work is the first to investigate the evolution of hotspots in degenerate matter with *realistic* turbulent conditions, so it is hoped that this analysis proves to be a step forward in this area. The present computational study and subsequent analysis confirms the intuition provided by Khokhlov but indeed raises even more questions concerning the ability of hotspots to form detonations in realistic conditions. These uncertainties motivate the next subject of the present work: the application of machine learning to this challenging problem.

CHAPTER 4

A DATA-DRIVEN MODEL FOR DDT

4.1 Introduction

Chapter 2 briefly reviewed past efforts at SGS modeling of DDT in thermonuclear SNe. These have relied on heuristic arguments for defining the DDT criteria.

In this chapter a novel type of SGS model for DDT is proposed that uses DNS of the detonation formation process to define the conditions for detonation formation on the LES scales. As identified in Chapter 1, one of the most likely modes of detonation formation in the unconfined turbulent flame is via the Zel'dovich reactivity mechanism. Thus the insight gained in Chapter 3 with respect to the Zel'dovich mechanism is leveraged to lay the foundation for the new model.

One key piece of the overarching goal of producing a SGS model for the full-star explosion models is the development of a model for characterizing reactive turbulence realizations in terms of the potential for creating detonation-prone hotspots. One possible way to achieve this goal is to develop a *classifier* capable of accurately classifying individual hotspots as either detonation-forming or non-detonation-forming.

To train the model on this task, the large database of simulations of realistic hotspot configurations from Chapter 3 is used. The physical insights gained in that chapter are used to determine which features to select for the model. At the end of the chapter, verification of the model's accuracy is performed using one-dimensional, reactive turbulence simulations on the scale Δ_{tb} of the `tburn` models.

4.2 Methods

Developing a SGS model to predict the onset of DDT from data resolved on the explosion filter scales, Δ_{wd} , requires the connection of physics between this scale and the lower end of the turbulent flame scale, Δ_{tb} . In Chapter 3 it was observed that on these scales hotspots can form and lead to detonations. Then the input data to a model for classifying the potential for hotspots must be on the scale of Δ_{tb} .

The collection of simulations of one-dimensional, planar hotspot configurations are used to construct a predictive model capable of identifying detonation-forming hotspots given an initial configuration. The classifier is given data samples of the form $\{(\boldsymbol{\chi}_i, f(\boldsymbol{\chi}_i))\}_{i=1}^{n_s}$, where n_s is the number of samples. Here $\boldsymbol{\chi}_i \in \mathbb{R}^{n_x \times n_c}$ is the i^{th} input to the classifier, n_x is the number of spatial cells and n_c is the number of input channels (e.g. flow variables). The label for sample i is given by $f(\boldsymbol{\chi}_i) \in \{0, 1\}$. A value of 0 indicates non-detonation-forming, and a value of 1 indicates detonation-forming.

Then the task of supervised machine learning is as follows,

$$\text{Given the measurements } \{(\boldsymbol{\chi}_i, f(\boldsymbol{\chi}_i))\}_{i=1}^{n_s}, \text{ approximate } f. \quad (4.1)$$

In the present work the function f in Equation (4.1) is essentially mapping an initial coarsened hydrodynamic state to a physical outcome and can thus be thought of as a parameterization of the nonlinear dynamics of the governing system of partial differential equations over the short time window.

The nonuniform initial conditions and highly nonlinear interaction between combustion and gas dynamics precludes a model based on simple parameterizations of the initial hotspot profile, such as its amplitude and width. In order to be generalizable to arbitrary initial configurations, it is expected that the model must be able to learn more complex features such as the critical gradients of induction time, the dependence on density, etc. (although the amplitude and width of the hotspot may still prove to be valuable features for learning).

To accomplish these objectives, the model makes use of deep neural networks (DNNs) which have been successful in solving certain classes of problems (for more information on using DNNs for function approximation, see [2] and references therein). In particular this work considers both artificial neural networks (ANNs) and convolutional neural networks (CNNs) [18] for the architecture of the present classification model. These have their own unique tradeoffs in terms of performance. With a CNN the focus is on learning the salient spatial features of the hotspot that lead to detonation. On the other hand, the ANN may be sufficient if pertinent features of the problem are extracted.

The learning process involves the training of network parameters on a set of training data that is representative of the problem at hand. Broadly speaking, the goal of the learning process is to produce a model with good generalizability, meaning that it is able to predict the outcome of new data samples not included in the training dataset. To measure how well the network is able

to generalize, a subset of samples is selected from the whole dataset, remove it from the training process, and pass it through the network once the network has been trained. This subset of data samples is referred to as the validation dataset (also sometimes called the test data).

The first step in building the network is to identify the appropriate features to use as inputs to the network. This determines the input dimensions and may also influence what type of architecture is to be used. The features chosen should effectively characterize the input data with as few dimensions as possible. This helps to keep the size of the network, in terms of the number of free parameters, as small as possible and may improve generalization.

4.2.1 Feature selection

For the feature selection step two main strategies are proposed. In the first strategy the spatial profiles of a select few flow quantities at the initial time are used. The network is tasked with learning the spatial features (i.e. gradients) necessary for detonation formation from this data. The second strategy utilizes the Khokhlov-inspired timescale analysis introduced in Chapter 3 as the input feature space. These two strategies are referred to as the *naive strategy* and the *Khokhlov strategy*, respectively.

Naive strategy. In the naive strategy, either the induction time profile or the reactive wave speed normalized by the soundspeed, denoted by $z = u_{sp}/c$, is used as the primary feature for training. This choice is based on prior experience in analyzing detonation formation in the context of the reactivity gradient mechanism. This strategy is referred to as naive because it considers only the raw flow quantity as a function of space and does not take into account any additional information that may be gathered from physical insight into the problem.

Two slightly different approaches are taken with respect to the different datasets. When training with the synthetic dataset, a radial section of the initial profile(s) is used as input, given that the profiles are symmetric. The dimension n_x of the input array χ is determined by the desired sampling rate. In particular, it will be determined by the ILES filter cutoff, Δ_{tn} , of the `tburn` models in which the network is to be employed.

Five models consistent with the naive strategy are proposed:

$$\text{N1} : \{\boldsymbol{\tau}\} \in \mathbb{R}^{n_x,1} \mapsto q \in \{0,1\}, \quad (4.2)$$

$$\text{N2} : \{\boldsymbol{\tau}, \boldsymbol{\rho}, \boldsymbol{c}, \boldsymbol{u}\} \in \mathbb{R}^{n_x,4} \mapsto q \in \{0,1\}, \quad (4.3)$$

$$\text{N3} : \{\boldsymbol{\tau}, \boldsymbol{\rho}, \boldsymbol{u}\} \in \mathbb{R}^{n_x,3} \mapsto q \in \{0,1\}, \quad (4.4)$$

$$\text{N4} : \{\boldsymbol{\tau}, \boldsymbol{c}, \boldsymbol{u}\} \in \mathbb{R}^{n_x,3} \mapsto q \in \{0,1\}, \quad (4.5)$$

$$\text{N5} : \{\boldsymbol{z}, \boldsymbol{\rho}, \boldsymbol{u}\} \in \mathbb{R}^{n_x,3} \mapsto q \in \{0,1\}. \quad (4.6)$$

The symbol N indicates that model belongs to the naive family of models. Model N1 is the most simple, using as input only the induction time and mapping to the (scalar) output label, q . Models N2 through N5 use either the log of the induction time, $\boldsymbol{\tau}$, or the normalized reactive wavespeed, \boldsymbol{z} as the sensor intended to capture the reactivity gradient mechanism. Then they also include density, $\boldsymbol{\rho}$, and/or soundspeed, \boldsymbol{c} . The inclusion of density is intended to account for the density dependence observed in Chapter 3. All models include the velocity, \boldsymbol{u} , to account for the effects of turbulent motions during the evolution.

In Figure 4.1 the normalized inputs of eight randomly chosen training samples from the TE dataset are shown. Here the training features (flow variables) are normalized by the smallest and largest occurring values in the dataset such that the range of the inputs is between 0 and 1. These five variables are the superset of the variables available to models N1 through N5.

Khokhlov strategy. Another feature selection strategy developed to solve Equation (4.1) is advised by the Khokhlov-inspired analysis in Chapter 3. The proper application of Equation (2.1) using the new criteria Equation (3.2) is able to effectively separate non-detonation-forming and detonation-forming samples in the reactive timescale versus sound-crossing timescale phase space, as seen in Figure 3.8.

In this strategy the *reactive timescale*, *sound-crossing timescale*, *density*, and *divergence of velocity* computed from the initial time are used as inputs. The latter two are taken to be the mean of the quantity over the region r_0 . The first three choices are obvious from the results of Figure 3.5. The choice of the divergence of velocity as an additional input parameter is made to take into account existing expansion or compression of the gas in the region of interest.

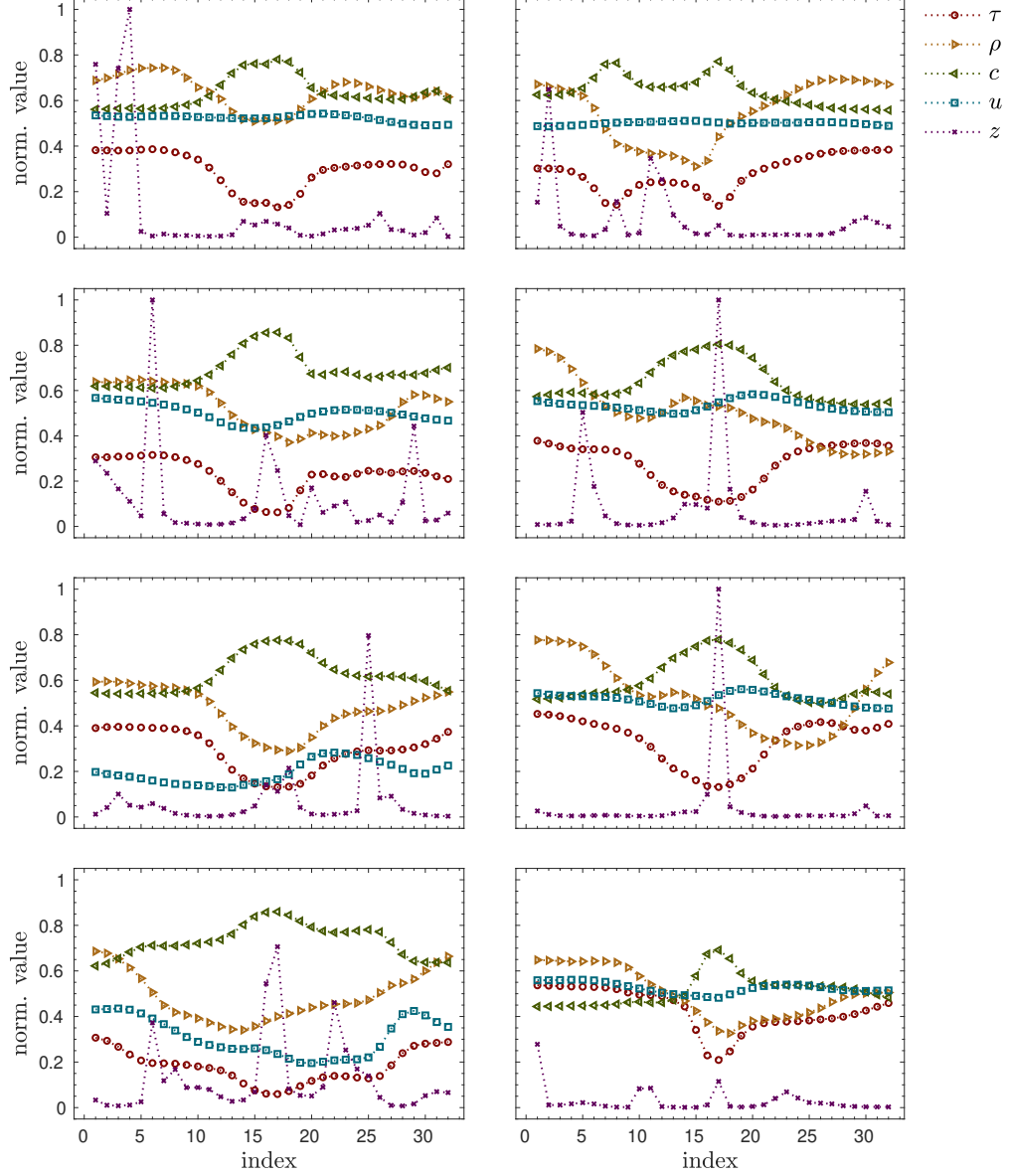


Figure 4.1: Normalized inputs from eight randomly chosen training samples. Shown in each panel is the normalized induction time (red circles), density (gold right-arrows), soundspeed (green left-arrows), velocity (blue squares), and z value (purple crosses).

The following two models are proposed, each consistent with the aforementioned Khokhlov feature selection strategy:

$$\mathbb{K}1 : \{\log_{10}(\sigma_0), \log_{10}(r_0/\langle c_0 \rangle), \langle \rho_0 \rangle\} \in \mathbb{R}^3 \mapsto q \in \{0, 1\}, \quad (4.7)$$

$$\mathbb{K}2 : \{\log_{10}(\sigma_0), \log_{10}(r_0/\langle c_0 \rangle), \langle \rho_0 \rangle, \langle \text{div } u_0 \rangle\} \in \mathbb{R}^4 \mapsto q \in \{0, 1\}. \quad (4.8)$$

Here, again, q is the binary output classification. The notation $\mathbb{K}1$ stands for ‘Khokhlov model 1’.

This model omits the divergence of velocity as input and is intended for use with the synthetic data only (again, all synthetic data have a velocity of zero everywhere in the domain). The model $\mathbb{K}2$ includes the divergence of velocity measurement and is intended for use with the TE data.

Given that a detonation may occur on either side of the non-symmetric hotspot in the TE models, it must be decided which side to extract timescale data from. In the present work, the ratio of the reactive timescale, σ_0 , to the sound-crossing timescale, $r_0/\langle c_0 \rangle$, is computed for both sides, and the ratio with the *lowest* value is selected. This value places the sample further toward the detonating portion of the timescale plane in Figure 3.8.

4.2.2 Neural network architecture

In terms of network architecture both ANNs and CNNs are considered. The ANN consists of several layers that sometimes referred to as a fully connected layers, as every unit in a layer applies a transformation to the output from each unit in the layer preceding it. The transformation is applied using weight values that later become the target of optimization. Each evaluation of a training sample produces a measure of error using a loss function. The updating of weights then involves the process of backpropagation, which calculates the gradient of the loss with respect to the weights and allows information about the performance of the network to improve the weights and biases.

The unit output of the ℓ^{th} fully connected layer in a network may be expressed mathematically as

$$q_j^{(\ell)} = \varphi \left(\sum_{i=1}^{n^{(\ell-1)}} w_{j,i}^{(\ell)} q_i^{(\ell-1)} + b_j^{(\ell)} \right), \quad (4.9)$$

where φ is a nonlinear activation function, $n^{(\ell)}$ is the number of units in layer ℓ , $w_{j,i}$ is the weight for the connection between unit j of layer ℓ and unit i of layer $\ell - 1$, and $b_j^{(\ell)}$ is the bias for unit j of layer ℓ [38].

The unit transformation equation, Equation (4.9), may be expressed in matrix form as $\mathbf{q}^{(\ell)} = \mathbf{w}^{(\ell)} \mathbf{q}^{(\ell-1)} + \mathbf{b}^{(\ell)}$. Then the feedforward ANN may be conveniently expressed as a series of layers acting in series such that the output of the final layer L may be expressed as

$$\mathbf{q}^{(L)} = \varphi \left(\mathbf{w}^{(L)} \varphi \left(\mathbf{w}^{(L-1)} \varphi \left(\dots \left(\mathbf{w}^{(1)} \boldsymbol{\chi} + \mathbf{b}^{(1)} \right) \dots \right) + \mathbf{b}^{(L-1)} \right) + \mathbf{b}^{(L)} \right). \quad (4.10)$$

Convolutional layers may also be included in this feedforward system. A convolutional layer applies a sliding filter across the input data to generate a feature map. The weights of this filter are

learned during the training process. In the naive strategy the input data is strictly one-dimensional, thus a one-dimensional convolutional layer must be applied. The 1D convolutional output unit is given by

$$q_j = \varphi \left(\sum_{i=1}^{n_x^{(\ell)}} \sum_{k=1}^{n_{ch}^{(\ell)}} w_{i,k} \chi_{j+i,j+k} + b \right), \quad (4.11)$$

where $n_x^{(\ell)}$ is the number of spatial points in the filter and $n_{ch}^{(\ell)}$ is the number of channels¹. Typically each channel of a filter is referred to as a kernel.

The basic architecture of the feedforward network for the naive strategy is illustrated in Figure 4.2. The inputs to the network are the spatial profiles of induction time, coarsened to the

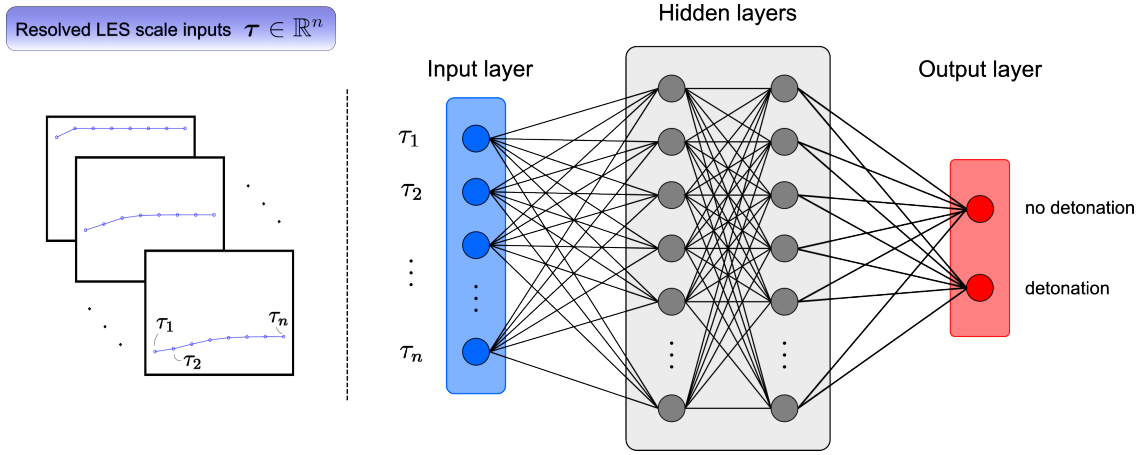


Figure 4.2: Overview of the neural network approach for the naive strategy, N1. The network input is the induction time profile computed via DNS, but coarsened to the Δ_{tb} cutoff resolution. The binary classification labels of ‘no detonation’ and ‘detonation’ are determined by the result of the corresponding DNS.

Δ_{tb} filter scale, and plotted in blue. The hidden layers, shown in the gray region, may consist of a combination of convolutional and fully connected layers or only of fully connected layers.

With the basic elements of network architecture established, details about the proposed network implementation are described next. These include the choice of activation function, loss function, solver, and more.

Activation functions. Activation functions are used to introduce nonlinearity into the machine learning model. There are many choices of activation functions available. Certain qualities can make some activation functions superior for backpropagation such as the problem of vanishing

¹Note that for the input layer the notation n_x and n_{ch} is used without superscripts for brevity

gradients. The rectified linear unit (ReLU), which does not suffer from the issue of vanishing gradients, is widely used and accepted as a de facto standard for most applications. The ReLU activation function is given by

$$\varphi(x) = \begin{cases} x, & \text{if } x > 0, \\ 0, & \text{otherwise.} \end{cases} \quad (4.12)$$

For all of the dense layers and convolutional layers used in the present model, ReLU activation function is used. Finally, following the output layer, a softmax function is applied. This scales the activations and ensures that the probabilities sum to unity.

Loss function. The binary cross-entropy loss function is used in all of the network implementations. The binary cross-entropy loss function is

$$\mathcal{L}_{\text{bce}} = -\frac{1}{n_s} \sum_{i=1}^{n_s} q_i \log(\hat{q}_i) + (1 - q_i) \log(1 - \hat{q}_i), \quad (4.13)$$

where, again, n_s is the number of samples, q_i are the labels and \hat{q}_i are the predicted label values.

Solver. Once the architecture is set, the weights and biases are computed using the `adam` [29] implementation in Keras. This algorithm is a type of stochastic gradient descent optimization scheme.

A scheduled learning rate is used that adjusts the learning rate, γ , during the learning process to reduce possibility of ‘overshoot’ once a local minima in the solution space is found. Once a minimum number of epochs has been reached, the learning rate is adjusted by multiplying the previous rate by $\exp(-0.01)$.

4.2.3 Performance metrics

The performance of the neural network models is assessed using several commonly used metrics. Given the true-positives, TP, false-positives, FP, true-negatives, TN, and false-negatives, FN, the accuracy is given as

$$\text{Accuracy} = \frac{\text{TP} + \text{TN}}{\text{TP} + \text{TN} + \text{FP} + \text{FN}}. \quad (4.14)$$

In binary classification the accuracy metric gives the ratio of the number of correct predictions to the number of total predictions made. The next metric considers the number of positive predictions (detonation-forming hotspots) that are actually true. This is the precision metric, given as

$$\text{Precision} = \frac{\text{TP}}{\text{TP} + \text{FP}}. \quad (4.15)$$

Similarly, the recall (also known as the sensitivity or true positive rate), which is the number of actual positive samples that are correctly identified by the classifier as such, is also used. The recall is given by

$$\text{Recall} = \frac{\text{TP}}{\text{TP} + \text{FN}}. \quad (4.16)$$

Finally the classification performance using a threshold-invariant and scale-invariant method known as the receiver operating characteristic (ROC) curve is considered. The ROC curve is comprised of many points on the Recall (also known as the sensitivity or true positive rate) versus false positive rate plane, with each point corresponding to a different threshold value. The integral of this function is known as the ‘area under the curve’ (AUC), and is used as a common metric in testing accuracy. For a perfect classifier the value of the AUC is 1.

4.2.4 Using the classifier as a subgrid-scale model

The primary use of the new classifier is as a component of a SGS model for DDT in full-star simulations of SN Ia. Referring back to Figure 2.1, the connection of scales relevant to DDT and the roughly 1×10^5 cm resolution of the full-star models is required. A two-component SGS model is proposed. The first component requires the new classifier to assign a probability of detonation formation for each hotspot produced by a given reactive turbulence realization on the Δ_{tb} scale. The predictions by the classifier are made during runtime of the model. The second component then involves another training process to assign to each reactive turbulence realization considered a probability of producing a DDT. Then, the idea is to apply this learned model during runtime of the full-star models to determine when and where a DDT is likely.

To this end, a kernel tracking algorithm is developed for Proteus and stored in a new module named `SubGridScaleDDT`. The program assigns unique ID numbers to prospective DDT kernels and tracks their movement during the simulation. If the properties of a prospective kernel meet user-defined criteria, then data is extracted from the vicinity of that kernel and passed to the trained neural network model of choice. The Proteus simulation code interfaces with the Python/Keras network model implementation using a package Python package known as CFFI (C Foreign-Function Interface). For more details on the embedding of the network model implementations, see Appendix C.

The `SubGridScaleDDT` module has some features that make it convenient to use. As stated, the module tracks the individual DDT kernels and their location between timesteps. Kernels are ranked in order of increasing minimum induction time, meaning that the kernels with the lowest

induction time are prioritized. While the number of kernels that can be tracked is very large, the number of kernels allowed to be evaluated can be set by the user, saving computational resources. The frequency of evaluations with respect to the timestep number may be user-adjusted, as well as the starting simulation time to begin evaluations.

When the naive strategy is used, the profiles of the appropriate quantities are extracted from the vicinity and passed to the network. In 1D this is trivial. In 2D or 3D the procedure stays conceptually the same, however now multiple ‘lineouts’, or 1D data strips are extracted at multiple angles for each kernel. The number of lineouts is user-determined. The rationale for this 1D lineout procedure is given by the inherently one-dimensional nature of the Zel’dovich reactivity gradient mechanism.

4.3 Results

With the neural network models defined as well as the metrics used to characterize their performance, the results of the training process are presented. At the end of the section results are presented of the numerical experiments in which the learned networks are used as a SGS model in ILES of reactive turbulence (in the `tburn` models) to predict the formation of detonations.

It is necessary to introduce a few specific training/validation datasets that can be used interchangeably with the neural network models. First the dataset `td.naive.synthetic` is defined which processes the results of the synthetic databases `GLtHt`, `GMdHt`, `GHvHt`, `GMdCd`, `GMdWm`, and `GRND` into the format readable for the naive network models `N1` through `N5`. The same databases are also combined into a dataset `td.khokhlov.synthetic` which processes the data into the format compatible with the Khokhlov strategy. Then the `TE` database is similarly processed into two training/validation datasets, `td.naive.turb` and `td.khokhlov.turb`.

4.3.1 Naive strategy

The communication of results begins with the training and validation performance of model `N1` on the synthetic dataset `td.naive.synthetic`. In this model the only input feature is the profile of induction time extracted from one half of the symmetric synthetic hotspot. The performance of the model over 200 training epochs is shown in Figure 4.3. The model achieves high scores in both Accuracy and AUC for the training and validation sets.

Next the model performance when additional features are included is presented. The models `N2` through `N5` are trained on the `td.naive.turb` dataset. A subset of this training dataset is

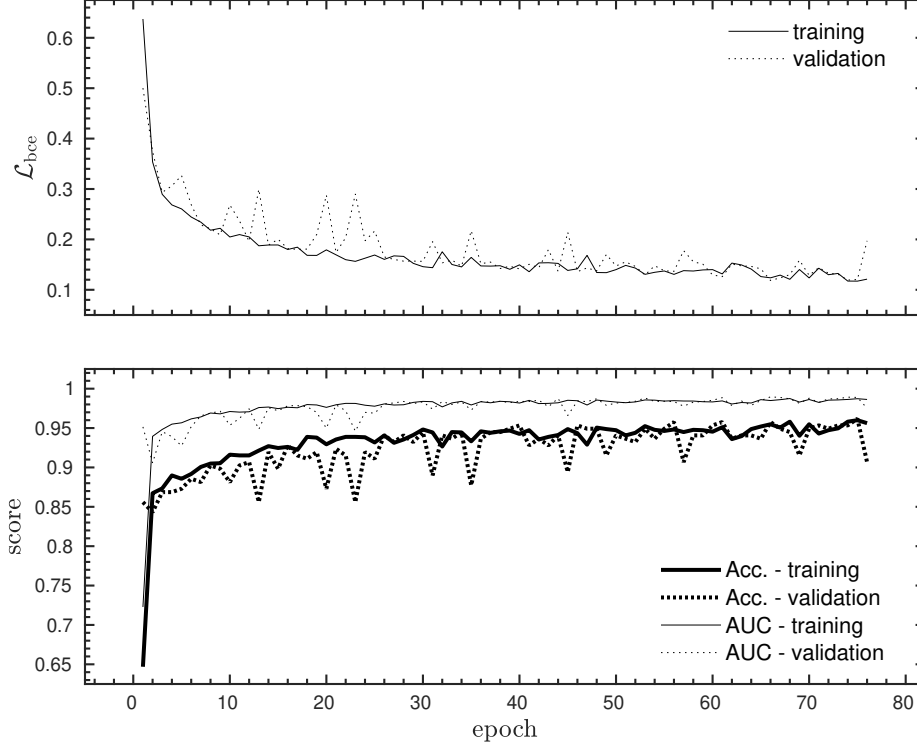


Figure 4.3: Training and validation loss (top panel) and accuracy metrics (bottom panel) for the $\mathbb{N}1$ model trained on the synthetic dataset, dataset `td.naive.synthetic`.

used to tune the hyperparameters of the model, and the process is documented in Appendix B. A summary of the results of the hyperparameter tuning process are included in Table 4.1. From these results it seems that the preferred number of filters for the two convolutional layers is 8 and 128, respectively. The filter width in each of the layers varies. The number of dense layers seems also to fluctuate, as does the number of nodes per layer.

These tuned models are trained and tested on the full `td.naive.turb` dataset over about 50 to 60 epochs, before early stopping is used. Early stopping is used in each of the models when improvement is no longer being made in the validation AUC score. The training and validation binary cross-entropy loss history is presented in Figure 4.4. The model $\mathbb{N}4$ achieves the lowest loss value on the validation set at the end of the training process, with a value of around $\mathcal{L}_{\text{bce}} = 0.16$. In fact the histories for both $\mathbb{N}2$ and $\mathbb{N}3$ achieve scores around this value earlier in their training as well. Notably, the performance of the model $\mathbb{N}5$ which uses the z value in place of the induction time, τ , is quite poor.

The training and validation AUC score histories for the four models are shown in Figure 4.5. It

Model	nfltrs	fltrs _{sz}	dopool	nnodes	drpout	nparams
N2	-	-	-	-	-	205,114
c _{lyr} _1	8	5	0	-	-	-
c _{lyr} _2	128	7	0	-	-	-
d _{lyr} _1	-	-	-	256	0	-
N3	-	-	-	-	-	267,362
c _{lyr} _1	8	3	0	-	-	-
c _{lyr} _2	128	3	0	-	-	-
d _{lyr} _1	-	-	-	128	0.25	-
d _{lyr} _2	-	-	-	512	0.25	-
N4	-	-	-	-	-	90,082
c _{lyr} _1	8	3	0	-	-	-
c _{lyr} _2	128	7	1	-	-	-
d _{lyr} _1	-	-	-	128	0.25	-
d _{lyr} _2	-	-	-	128	0.25	-
N5	-	-	-	-	-	660,962
c _{lyr} _1	8	3	0	-	-	-
c _{lyr} _2	128	3	1	-	-	-
d _{lyr} _1	-	-	-	512	0	-
d _{lyr} _2	-	-	-	512	0	-

Table 4.1: Summary of the network architectures resulting from the hyperparameter tuning process. For each of the four models, N1, N2, N3, and N4, the table shows the number of convolutional filters (`nfltrs`), filter size (`fltrssz`), use of pooling (`dopool`), number of dense layer nodes (`nnodes`), and dropout percentage (`drpout`). The n th convolutional layer is labeled as `clyr_n`, and the n th dense layer is labeled as `dlyr_n`.

is observed that for the validation AUC score, again models N2, N3, and N4 perform very similarly. Note that the final weights for these models are taken from the epoch with the best validation AUC score.

In an effort to visualize to some extent the workings of the network, the 8 filters of the first layer comprising the N2 model are shown in Figure 4.6. In this figure each of the filters 1 – 8 are ‘unwrapped’ along the columns, showing the kernels of the filter corresponding to each input channel. In order, the columns show the learned weights of the kernels for induction time, density, soundspeed, and velocity.

4.3.2 Khokhlov strategy

Next, the performance of the model employing the Khokhlov strategy is examined. The first results presented are of the model $\mathbb{K}1$ trained on the synthetic dataset, `td.khokhlov.synthetic`. A 10 percent data split is used for the validation set. In Figure 4.7 the training and validation

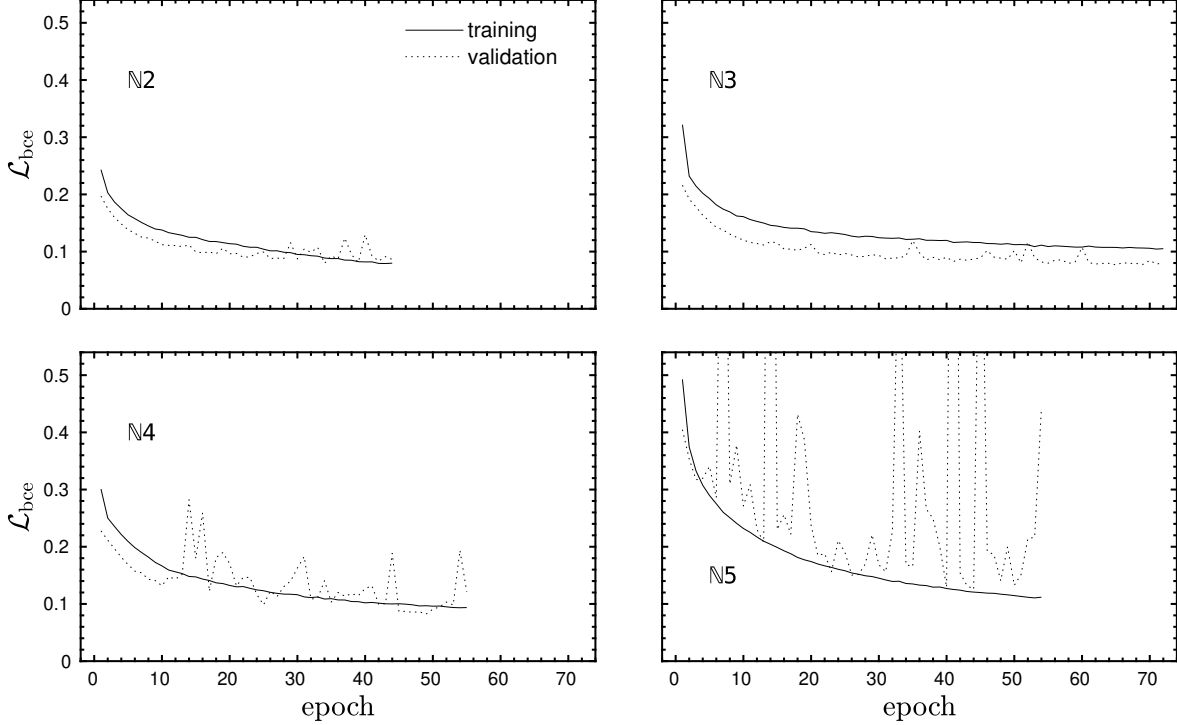


Figure 4.4: Comparison of the training and validation loss for the N2 (top left panel), N3 (top right panel), N4 (bottom left panel), and N5 (bottom right panel) models on the `td.naive.turb` dataset.

loss is plotted (top panel) as well as the accuracy scores (bottom panel). Next, the Accuracy (abbreviated `Acc.` in the legend) and AUC scores are examined for the training and validation data. An essentially perfect AUC score is observed on the validation data at epoch 194. At the same epoch it is observed that Accuracy ≈ 0.99 .

Then the performance of model `K2` trained on dataset `td.khokhlov.turb` is presented. In Figure 4.8 the training and validation loss is shown (top panel) along with the Accuracy and AUC scores (bottom panel). The training and validation loss display similar convergence, indicating that the model is generalizing adequately well and not ‘overfitting’. The same property is observed in the accuracy scores. Even for the more complicated dataset the current approach is able to predict about 91 percent of validation samples correctly. The maximum AUC score attained is about $\text{AUC} = 0.97$.

4.3.3 Performance summary

In Table 4.2 the training performance is summarized across the models and dataset combinations considered. Values are rounded to the nearest thousandth. Besides the slightly worse performance

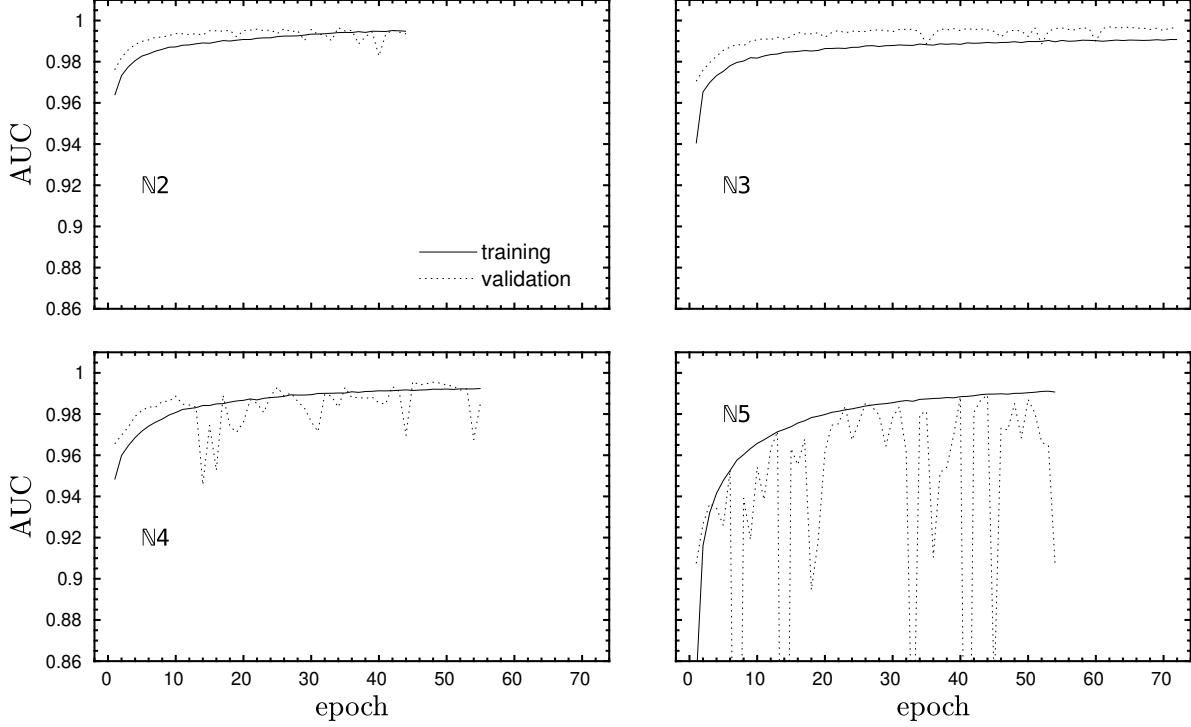


Figure 4.5: Comparison of the AUC metric on the training and validation data for the N2 (top left panel), N3 (top right panel), N4 (bottom left panel), and N5 (bottom right panel) models on the `td.naive.turb` dataset.

Strategy	Dataset	Accuracy	Precision	Recall	AUC
N1	<code>td.naive.synthetic</code>	0.958	0.936	0.983	0.990
N2	<code>td.naive.turb</code>	0.971	0.976	0.974	0.997
N3	<code>td.naive.turb</code>	0.971	0.973	0.978	0.997
N4	<code>td.naive.turb</code>	0.964	0.961	0.978	0.996
N5	<code>td.naive.turb</code>	0.947	0.935	0.977	0.989
K1	<code>td.khokhlov.synthetic</code>	0.987	0.983	0.991	1.0
K2	<code>td.khokhlov.turb</code>	0.911	0.924	0.928	0.973

Table 4.2: Summary of results for the methods introduced in Equations (4.2) to (4.6) and Equations (4.7) to (4.8) on the validation samples from datasets `td.naive.synthetic`, `td.naive.turb`, `td.khokhlov.synthetic`, and `td.khokhlov.turb`

of the N5 feature selection strategy, the naive strategies perform quite similarly. The Khokhlov feature selection strategy performs well on the realistic data, but not quite as well as the naive strategies do.

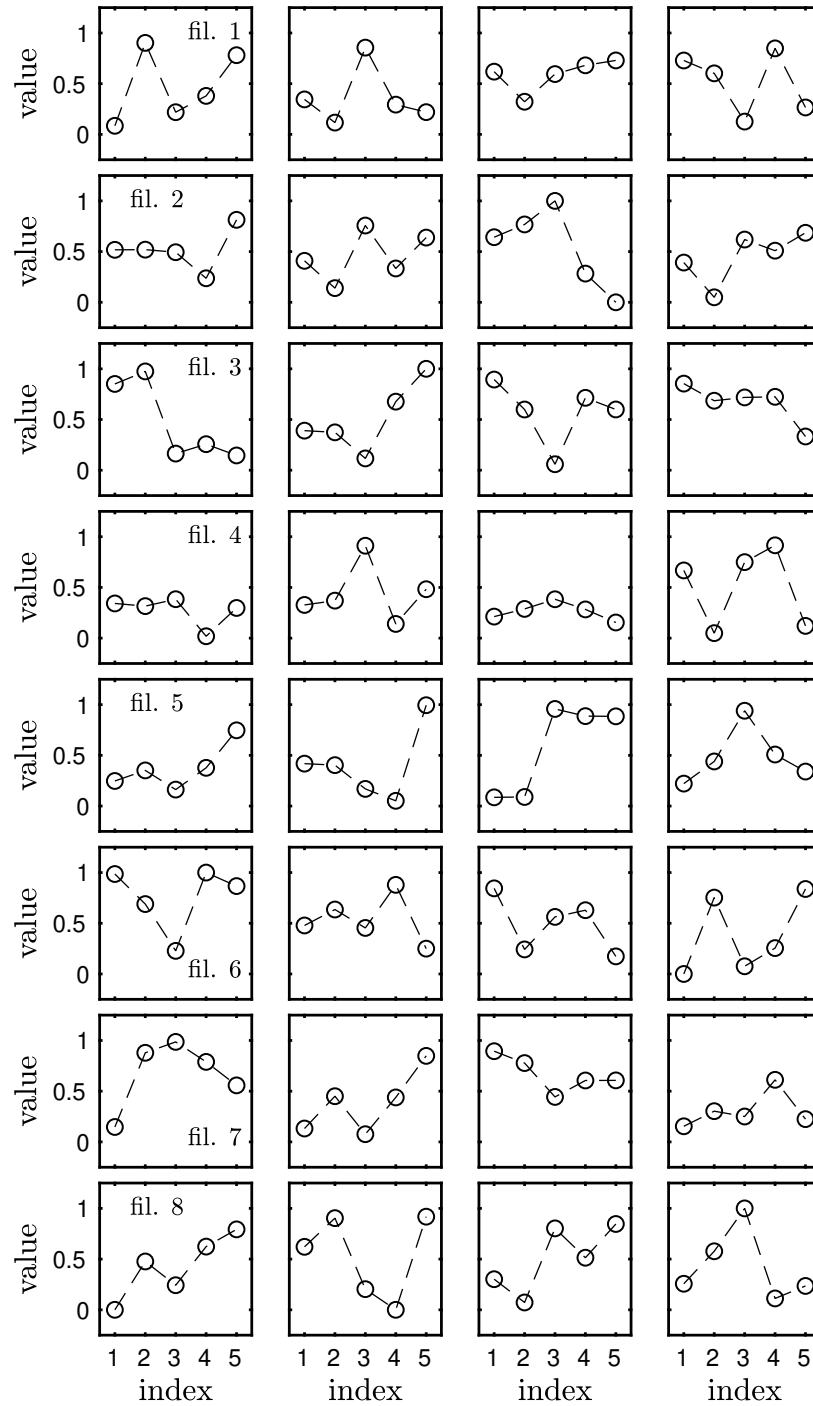


Figure 4.6: Weights for filters 1 – 8 of the first layer of model N2 are plotted, with each row comprising one filter and the individual kernels for inputs of induction time, density, soundspeed, and velocity spanning the columns. For plotting convenience, weights are normalized across filters for each input channel.

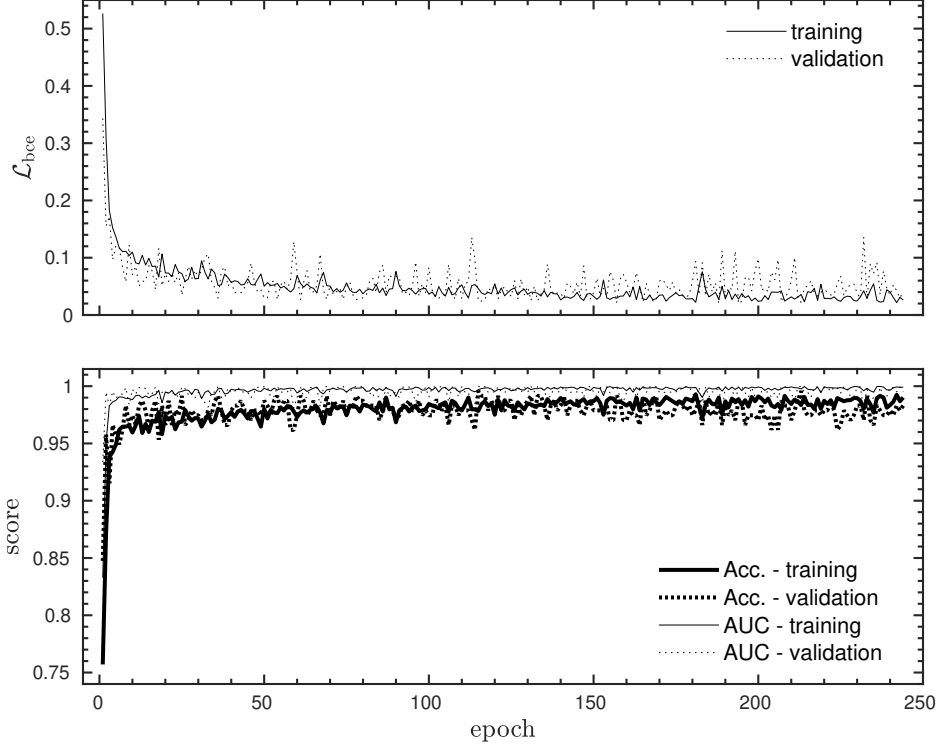


Figure 4.7: Training and validation performance of the $\mathbb{K}1$ model trained on the synthetic dataset, dataset `td.khokhlov.synthetic`. The network achieves a very high Accuracy score for the training (thick solid black line) and validation (thick dotted black line) datasets. Also the AUC score is near the maximum score possible of 1 for both datasets (thin solid blue line and thin dotted blue line).

4.3.4 Verification of the subgrid-scale model in the *a posteriori* setting

Verification testing of the trained neural network models is done in the *a posteriori* setting. The networks are employed as SGS models in semi-realistic, one-dimensional reactive turbulence. These turbulence simulations use the same setup as the `tburn` models except that they are of course one-dimensional. The turbulence is driven in 3 dimensions using the TurbGen code [15]. The 3D driving routine computes velocities across all three components, with the idea being to introduce some of the axial physics of turbulence into the 1D evolution. The use of 1D turbulence simulations in the verification process is intended to save time over fully 3D simulations, allowing more verification studies to be run and better statistics of performance to be obtained.

Through trial and error the turbulence driving parameters are adjusted to produce conditions that replicate some of the important statistics of 3D turbulence as closely as possible. Firstly, the turbulence is driven with a power law of $k^{-5/3}$, where k is the wavenumber. The target velocity

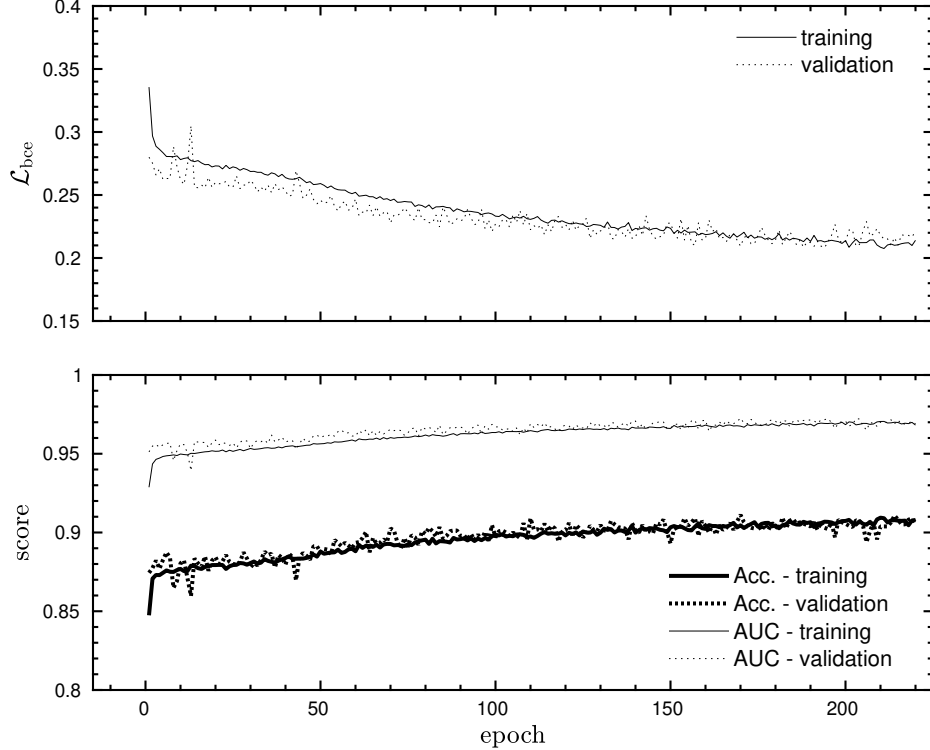


Figure 4.8: Training and validation performance of the $\mathbb{K}2$ model trained on the turbulence extracted dataset, dataset `td.khokhlov.turb`.

dispersion is 0.150×10^8 cm and the target RMS Mach number is around 0.05. While these velocities are below what is expected in 3D, they are about as high as they can be in 1D without producing strong shockwaves that initiate detonations before the Zel’dovich mechanism has a chance to occur. In Figure 4.9 some of the salient quantities are plotted over about 0.25 autocorrelation times (here the autocorrelation time is $t_{\text{turb}} \approx 0.213$ s). The compensated kinetic energy spectrum (top right panel of Figure 4.9) scales well with the expected power law up to a wavenumber of about 30, where numerical dissipation begins to take over, marking the end of the ‘inertial range’. The velocity components remain in a similar range due to the use of carefully selected amplitude adjustment factors. The temperature is initially set to $T = 1.55 \times 10^9$ K. Self-heating raises the temperature closer to the ignition temperature during the evolution, and eventually a detonation occurs.

The evaluation of the network models is performed during the reactive turbulence realizations. The best performing models are selected for this verification process. In particular, the naive strategy, $\mathbb{N}2$, and the Khokhlov strategy, $\mathbb{K}2$. Both of these network models are trained using the dataset with realistic conditions.

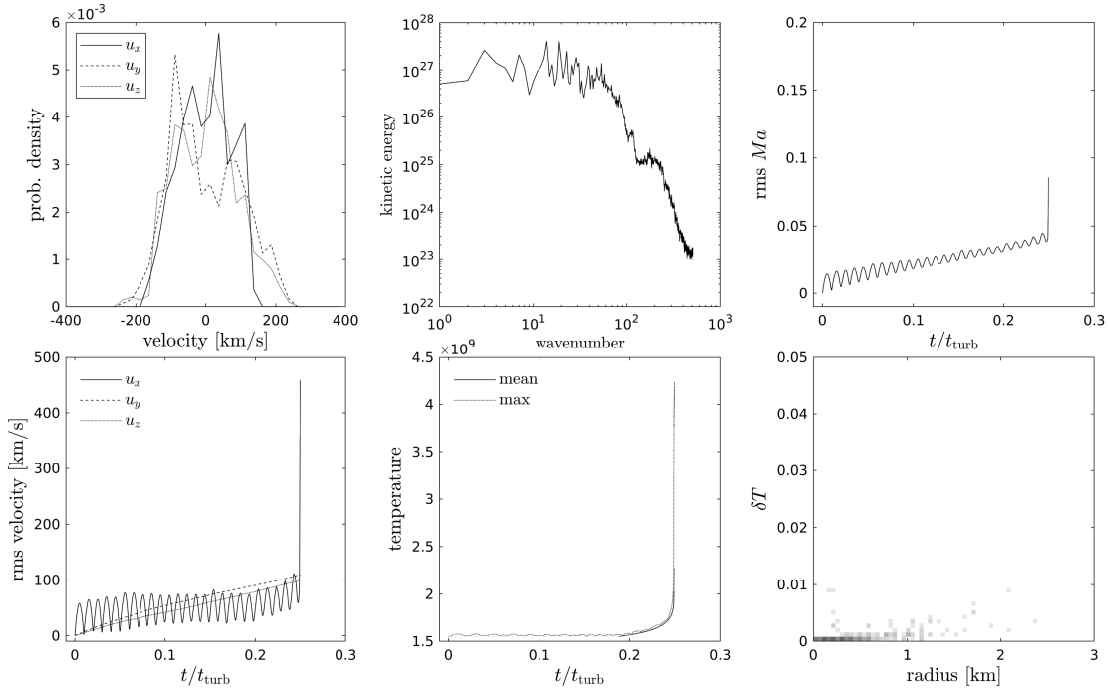


Figure 4.9: Overview of 1D turbulence used for verification studies. Shown is the probability density of velocities collected over 125 time samples (top left panel); the kinetic energy spectrum (top right panel) collected over the same number of samples, compensated by multiplying with $k^{5/3}$, where k is the wavenumber; the evolution of the RMS Mach number (middle left panel) the three velocity components (middle right panel), and the mean and maximum temperature (bottom left panel); and finally a bivariate histogram of amplitudes and widths of temperature fluctuations (bottom right panel) with higher frequency indicated by darker color.

To establish meaningful statistics, the turbulent realizations are run 64 times, each with a unique random seed. The network models evaluate potential detonation-forming hotspots during the evolution and compute a predicted probability of detonation for each one. The temporal accuracy of the predictions is assessed by measuring the time delay, δ_t , between the time when the prediction is made and the time of the detonation birth. Naturally, some time delay is expected. The spatial accuracy is assessed by measuring the distance, δ_x , from the point where the prediction is made to the *predicted* initial location of the hotspot center. This predicted location is computed by tracing the characteristics of the detonation backwards.

First, the model N2 is considered. Figure 4.10 shows the network predicted detonation probability, with the value shown in color, on the δ_t - δ_x plane. The predicted values at or near 1 (indicating a strong confidence in a detonation occurring) are concentrated near the origin of the plot as they

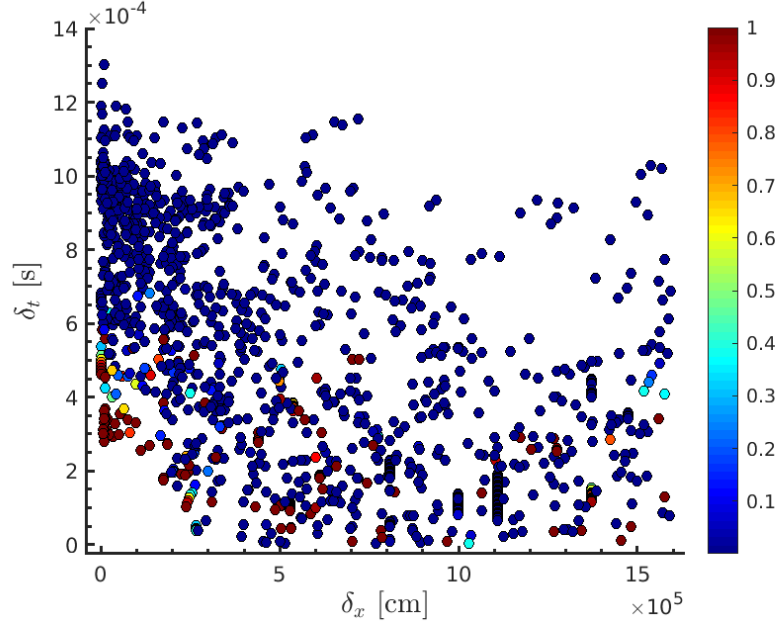


Figure 4.10: Results of the verification process for the naive model N2. Shown are the network predicted detonation probabilities (shown in color) on the δ_t - δ_x plane.

should be. The time delays are concentrated between 2.5×10^{-4} s and 4×10^{-4} s. This is on the order of the amount of time for a detonation wave to develop (see Figure 3.3 for reference). The points of high probability spread away from $\delta_x \approx 0$ may be false positives; those with δ_t being less than the detonation delay time may also be true positives, only that the simulation is terminated once the first detonation is born.

Next, the model K2 is evaluated for the same series of reactive turbulence realizations. Figure 4.11 shows the predictions in the δ_t - δ_x plane. Again, a concentration of predicted values of 1 is seen near the origin as in Figure 4.10. This indicates that the ability of the model to positively identify actual detonation-forming hotspots is satisfactory. However, there are undoubtedly many false positive predictions throughout the plane. It would seem that the Khokhlov strategy is less suited to distinguishing between detonation-forming and non-detonation-forming hotspots. Rather it seems to be identifying the necessary, but not sufficient condition for detonation to occur.

4.4 Discussion

In this chapter several novel strategies were introduced for predicting the onset of detonation formation among hotspots in reactive turbulence. The results of several tens of thousands of direct

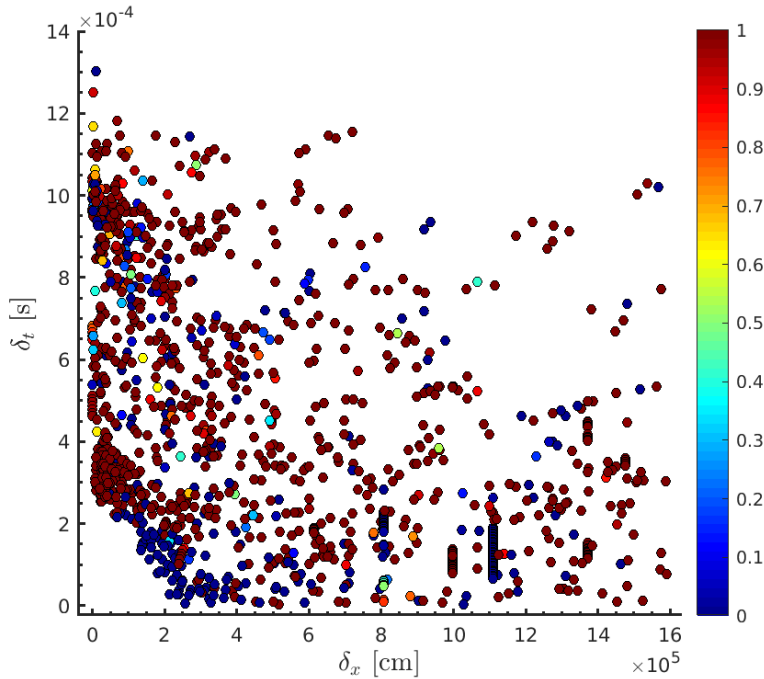


Figure 4.11: Results of the verification process for the Khokhlov model $\mathbb{K}2$. Shown are the network predicted detonation probabilities (shown in color) on the δ_t - δ_x plane.

numerical simulations of hotspot configurations were processed to produce training data for the NN-based strategies. The timescale analysis of Khokhlov [27] was used to parameterize the input space, allowing for a low-dimensional input space to be learned by the network.

Some observations on the performance of the two feature selection strategies are provided. First, it seems as though the performance of the Khokhlov strategy on the realistic dataset is, comparable to, but ultimately inferior to the naive strategies. One possible explanation for this finding is that the Khokhlov strategy does not consider pointwise data but rather statistical quantities computed from data within the center of the hotspot region. Perhaps some information that is highly correlated to the potential for detonation formation is lost in the process of averaging, such as the local gradients. In the naive approach these local gradients are potentially learned during the network training.

Another possibility is that the current realization of the Khokhlov strategy is simply lacking some additional statistical quantities. For example, it may be beneficial to supplement the input space with quantities such as the variance of densities in the region, or the mean Mach number

to incorporate information about the mean flow. The potentially missing information can only be determined by additional exploratory studies such as the ones undertaken in the present work.

4.4.1 On the use of the classifier as a subgrid-scale model

Next the potential of the classifiers to be effectively used as SGS model in the *a posteriori* setting is discussed. In the machine learning and ‘data science’ communities there are some general standards for ruling that a classifier has sufficiently learned a task. For a dataset whose labels are not significantly skewed, an Accuracy score of above 80 percent may be considered ‘good’, and a value above 90 percent may be considered ‘excellent’. Note that the target application of reactive turbulence is an inherently stochastic process, and a given realization of reactive turbulence that is close to a ignition may produce multiple potential detonation-forming hotspots nearly simultaneously. Thus there is no requirement to correctly classify every single one. Instead the aim is for the neural network classifier to provide us with a general measure, or probability, of how likely that particular realization is to produce a DDT. In other words, the results of the present work, particularly the results of Figure 4.10 and Figure 4.11, suggest that the output of the classifier be used as part of a statistical model rather than a deterministic one.

4.4.2 Notes on convergence of network accuracy

Finally some consideration is given to the issue of convergence of network accuracy with respect to the number of samples. This issue is pertinent for future work that considers the generation of a new, multidimensional dataset, as expanding the DNS of hotspot evolution to 2D or 3D will require roughly $4\times$ or $8\times$ computational cost. Thus it is important to provide an accurate assessment of the amount of computational work required to train a new network.

The convergence of network accuracy is explored by running numerous training procedures for varying number of samples, n_s , while keeping the number of validation samples fixed at around 2000 for each case. For each value of n_s , seven trials are run. The samples that are not in the validation set are eligible to be included in the training set during each trial, and that set is determined randomly. The same validation samples are used for each new trial.

In Figure 4.12 the convergence of network accuracy is shown with respect to the number of training samples. For the naive strategy, a sharp initial rate of increase is observed. The accuracy for the Khokhlov strategy is initially higher but the rate of increase is significantly less than that of the naive strategy initially. This suggests that Khokhlov strategy is able to generalize better

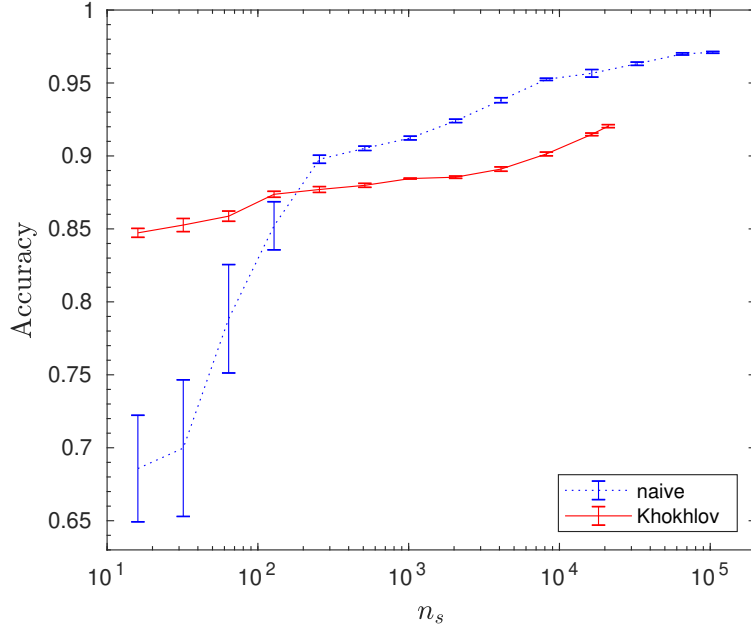


Figure 4.12: Convergence of network accuracy with the number of training samples.

with fewer number of training samples. However the naive strategy seems to differentiate better between non-detonation-forming and detonation-forming hotspots with increasing n_s . Note that the larger number of samples used for the naive approach is due to the data augmentation procedure introduced in Section 3.2.2.

CHAPTER 5

SUMMARY

In this work the problem of detonation initiation within hotspots in degenerate matter is addressed. The leading theoretical and computational evidence suggests that hotspots are likely to cause detonation of carbon fuel during a Type Ia supernova under certain conditions and assumptions. Based on the existing literature and the present work, it is speculated that these hotspot-induced detonations occur due to the Zel'dovich reactivity gradient mechanism. The Zel'dovich reactivity mechanism postulates that critical gradients of induction time are required near the hotspot in order for a 'spontaneous wave', generated near the center of the hotspot, to couple to the outgoing compressive wave, which is generated due to overpressure. If the critical gradient conditions are met then there is a chance for the coupling to succeed and create a positive-feedback loop where the reactive/spontaneous wave and the compressive wave reinforce each other through the compression and expansion of gas, forming a detonation.

In this study, results available in the literature were confirmed, and for the very first time simulations of hotspots with realistic background conditions were performed. This was done by extracting profiles from three-dimensional turbulence and using them as the initial conditions for direct numerical simulations of hotspots. The results indicate that despite best efforts, the outcome of the simulation cannot be decided by a simple parameterization.

To 'learn' the features of the hotspot that lead to the formation of a detonation wave, a novel neural-network based strategy was introduced. The networks were successfully trained on the large database of DNS studies used in the previous analysis. The network learning procedures demonstrated high Accuracy and AUC scores for both the training and validation sets. Finally the use of the trained networks as a subgrid-scale model in reactive turbulence was investigated. It was found that the models were able to predict the onset of DDT.

One of the major highlights of the present work is the large database of DNS studies of realistic hotspot configurations. Together with the newly proposed network approaches and future tweaking of the feature selection step as well as the network architectures, even better results could be achieved. An area where more work can be done if computational resources are available is in the

generation of even more DNS studies of hotspot configurations. In particular, it would be most beneficial to expand the range of ambient densities in these models.

Of course, one of the most obvious limitations of the studies is the restriction of the DNS of hotspots to one spatial dimension. While the Zel'dovich mechanism is inherently a one-dimensional mechanism, the presence of curves, or channels in the induction time field is expected to complicate the situation. These types of convoluted induction time channels are not uncommon in the distributed burning regime, and require special attention in any future work on this subject.

When it comes to generating new training data for more advanced models, an active learning approach [53] may prove very beneficial, especially if multi-dimensional DNS of hotspots is to be performed. Such studies would be very costly, and rather than sample the input parameter space randomly, it would be more time-efficient and resource-efficient to sample in regions where the network has the greatest uncertainty. In this work, the convergence of the network with respect to the number of training samples was presented, providing a useful estimate of the cost of developing new databases of DNS hotspot simulations.

APPENDIX A

ANALYSIS OF TURBULENT PERTURBATIONS

In this appendix the statistics of temperature perturbations in three-dimensional reactive turbulence simulations is presented. This information is used to guide the design of computational hotspot experiments, as the hotspot configurations studied should reflect the physical system as closely as possible.

In Figure A.1 four bivariate histograms of the amplitudes and radii of temperature perturba-

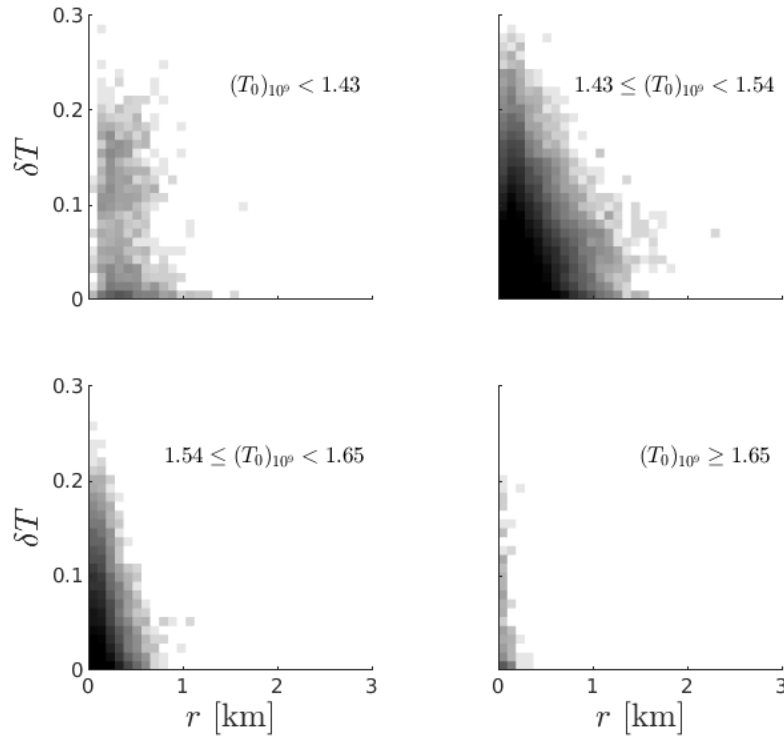


Figure A.1: Statistics of temperature perturbations near the end of the self-heating phase in three-dimensional reactive turbulence simulations. The distributions are categorized into four temperature ranges.

tions from a 3D reactive turbulence model are shown. The bivariate histograms each consider perturbations with ambient temperatures that are within a range of values. The first range is

$T_{\text{amb}} < 1.43 \times 10^9$ K, the second is $1.43 \times 10^9 \text{ K} \leq T_{\text{amb}} < 1.54 \times 10^9$ K, the third is $1.54 \times 10^9 \text{ K} \leq T_{\text{amb}} < 1.65 \times 10^9$ K, and the fourth is $T_{\text{amb}} \geq 1.65 \times 10^9$ K.

Given that the ambient density in the model is approximately $1 \times 10^7 \text{ g cm}^{-3}$ this means that temperatures below 1.43×10^9 K are very cold and not near ignition. For the perturbations with ambient temperatures in the range of 1.43×10^9 K through 1.54×10^9 K, the peak temperature can reach around 2×10^9 K. The perturbations with ambient temperatures in the range of 1.54×10^9 K through 1.65×10^9 K are in the detonation range with peak temperatures around 2.1×10^9 K.

Next the short induction time regions of the profiles extracted from three-dimensional turbulence used to form the TE database of simulations are analyzed. A regression analysis is performed using the Matlab fitting routine, `fit`, on each profile. The fit is performed with a Gaussian function with amplitude, a , mean value, b , and standard deviation, c . In Figure A.2 the probabilities of fitted

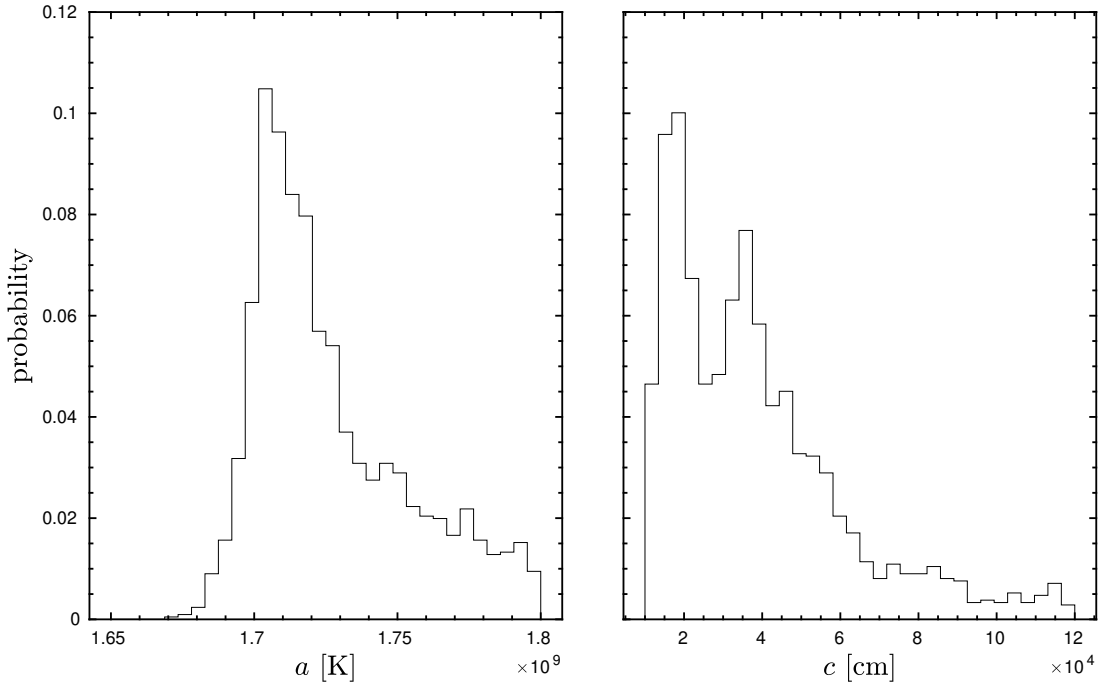


Figure A.2: Histograms of the calculated amplitude (left panel) and standard deviation (right panel) of the fitted functions to the turbulence extracted profiles.

amplitude and standard deviation values from the turbulent profiles are presented. The majority of fitted amplitudes are at around 1.7×10^9 K, with values reaching as high as 1.8×10^9 K for the samples considered. The radii of the perturbations are of greater interest. It is observed that the greatest concentration of perturbations are small, with standard deviation values of roughly 2×10^4 cm. Then the distribution decays with the exception of another smaller concentration at

around 3.5×10^4 cm. The tail of the distribution extends to about 1.2×10^5 cm; perturbations this large are in significantly smaller concentrations.

The choice of a Gaussian for describing the natural perturbations in the reactive turbulence data is examined. The R^2 goodness-of-fit statistic is used for this purpose. In Figure A.3 we show the

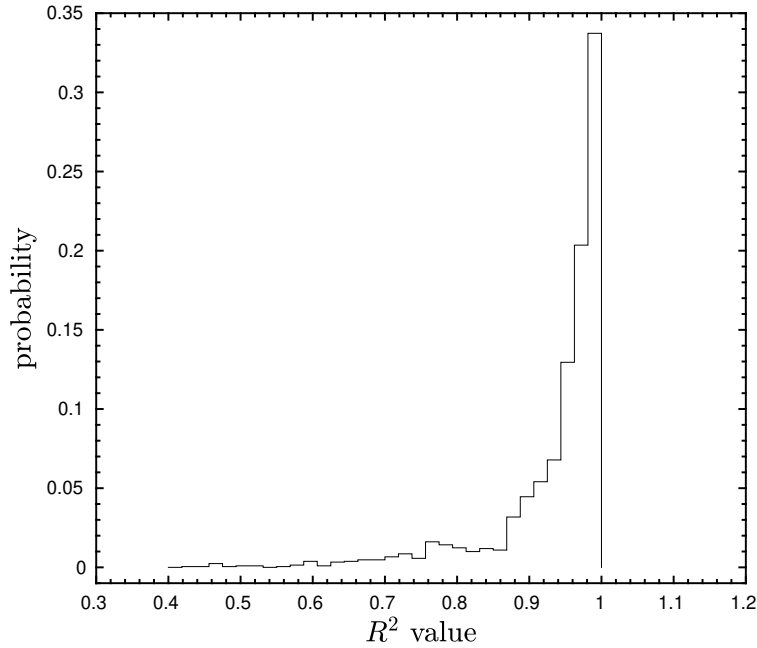


Figure A.3: Histogram of the R^2 goodness-of-fit statistic for the fitted functions to the turbulence extracted profiles.

R^2 goodness-of-fit statistic, also computed in Matlab, for the fitting process just described. An R^2 value of 1 is ideal, whereas lower values indicate greater deviation of the shape of the perturbation from a Gaussian. It is observed that the R^2 value is above 0.9 for the majority of fits. This result provides good support for the use of a Gaussian as the initial condition for the synthetic hotspots. However the tail region of the distribution motivates the study of hotspots with realistic initial conditions.

APPENDIX B

DATA PREPARATION, DATA AUGMENTATION, AND HYPERPARAMETER TUNING

B.1 Data preparation

The range of values of the inputs to the neural networks is very large. Between the induction time and density for instance, values span roughly 12 orders of magnitude. The induction time itself may range from around 10^{-5} s to greater than 10^{-1} s for a single input sample. These input data must be appropriately scaled before being passed to a neural network.

The appropriate scales are determined by computing the maximum and minimum values for each variable over all of the input samples. The inputs are scaled between these values such that the minimum and maximum of the new values are between 0 and 1. To treat the wide range of values in the induction time and some other quantities, log-scaling is used.

B.2 Data augmentation

Data augmentation strategies are employed in a few instances in the present work. The first use is in the evaluation of hotspot configurations to be simulated. To construct the turbulence extracted (TE) database, a total of 933 profiles are extracted from a 3D reactive turbulence dataset. These conditions are not simulated directly as their temperature in some cases is too low to achieve rapid burning. First a linear scaling of the temperature is applied to the original extracted temperature profiles, creating several offshoot models. The temperature is modulated such that the maximum lies between 2.0×10^9 K and 2.3×10^9 K. These new profiles form the TE database.

Before the process of training on the `td.naive.tburn` dataset, another form of data augmentation is utilized. This occurs during the downsampling process from the high-resolution DNS data to the Δ_{tb} scale. The cell averaging window is shifted slightly during the downsampling of interpolated profiles in order to (1) create more offshoot training samples and (2) hopefully improve the generalizability of the trained networks.

Parameter	Description	Range
<code>nclyrs</code>	number of conv. layers	[1, 2]
<code>nfltrs</code>	number of filters	[3, 5, 7]
<code>fltrsiz</code>	filters size	[8, 16, 32, 64, 128]
<code>dopool</code>	use pooling or not	[0, 1]
<code>ndlyrs</code>	number of dense layers	[8, 16, 32, 64, 128]
<code>nnodes</code>	number of units/nodes	[0, 128, 256, 512]
<code>drpout</code>	percentage of dropout	[0, 0.25, 0.5]

Table B.1: Summary of hyperparameters allowed to change freely, and the range of values that they are allowed to assume in the hyperparameter tuning process.

B.3 Hyperparameter tuning

The tuning of CNN hyperparameters is performed using the Keras Tuner [44] Python library. A subset of the training and validation samples was used for this tuning procedure, with the training set and validation set each having a ratio of detonating cases to non-detonating cases of about 65:100.

The CNN architecture hyperparameter tuning routine considered as variables the number of convolutional layers, the number of convolutional filters (varying independently), the filter size (also varying independently), the number of fully connected layers, the number of nodes per layer (varying independently), and the percentage of dropout. The dropout is set to be the same for each layer. The summary of hyperparameters is included in Table B.1. The *BayesianOptimization* routine (see [56]) is run for each of the four input models involved in the tuning process: N2 N3, N4, and N5. The AUC score averaged over several of the previous epochs is used as a tuning objective function. The number of training epochs per trial is 40.

APPENDIX C

NEURAL NETWORK MODEL EVALUATION IN PROTEUS

In this appendix the custom-made Fortran and Python software routines used to track and evaluate prospective DDT hotspots (hereafter referred to as kernels) during runtime of the Proteus simulation are described. These routines are part of an add-on package for Proteus called `SubGridScaleDDT`.

The `SubGridScaleDDT` software exists as a module of `physics/sourceTerms` in Proteus and can be included in the code by adding its path to the ‘Config’ file before simulation setup. The purpose of the main routine, `SubGridScaleDDT.F90`, is to find all of the prospective kernels at the current timestep. To do this a call is made to `SubGridScaleDDT_findAllKernels`. This routine searches through the simulation domain for computational cells satisfying a user-specified minimum induction time (cells with induction time values above this are unlikely to detonate and not worth tracking). The prospective DDT kernel is identified by evaluating first and second derivatives of induction time over the entire adaptive mesh refinement block to determine whether or not a point is a local minimum. Once a local minimum is found the kernel is added to the tracking list and given a unique tracking ID. The pseudo-code implementation is included in Algorithm 1. Once it is determined that a kernel is a local minimum of induction time, then for

Algorithm 1 Track and evaluate prospective DDT Kernels.

```
call SubGridScaleDDT_findAllKernels()
for all blocks do
  call SubGridScaleDDT_findLocalMinima()
end for
for all kernels do
  call SubGridScaleDDT_evalKernel()
end for
```

the naive strategy an array consisting of nearby cells, centered about the minimum, is extracted by the routine `SubGridScaleDDT_getLineout`. This extracted array is then passed to the routine `SubGridScaleDDT_callNN`. This routine serves as a wrapper around the python caller.

The neural network implementation uses the Python package, Keras. Keras serves as a front-end to the Tensorflow library. In order to embed the trained network in the runtime execution of the Proteus simulation code, the Python package CFFI (C-foreign function interface) was utilized. The CFFI package generates C code that exports the user's application programming interface (API) to a shared object library file. This library file can then be linked to any Fortran or C program.

The first step toward using the Python CFFI to build the C headers and dynamic shared object library file for Proteus is to edit the `nn_builder.py` script. In this script the desired Keras model name and appropriate inputs and outputs must be defined. Running the `nn_builder.py` script automatically generates the C header, C code, and shared object library file.

Once the necessary files are built, there are several steps required before running Proteus with the SubGridScaleDDT module and neural network model active. First the shared object library file must be added to the shared library path shell variable, `LD_LIBRARY_PATH`. Second, the Keras model directory must be copied in the directory where the executable is expected to be run. Once these steps are completed the Proteus executable is ready to be run.

BIBLIOGRAPHY

- [1] G. Abouseif and T. Toong. On direct initiation of gaseous detonations. *Combustion and Flame*, 45:39–46, 1982.
- [2] B. Adcock and N. Dexter. The gap between theory and practice in function approximation with deep neural networks. *SIAM Journal on Mathematics of Data Science*, 3(2):624–655, 2021.
- [3] W. D. Arnett. A Possible Model of Supernovae: Detonation of ^{12}C . *Astrophysics and Space Science*, 5(2):180–212, 1969.
- [4] A. Aspden, N. Nikiforakis, S. Dalziel, and J. Bell. Analysis of implicit LES methods. *Communications in Applied Mathematics and Computational Science*, 3(1):103 – 126, 2008.
- [5] A. J. Aspden, J. B. Bell, and S. E. Woosley. Distributed Flames in Type Ia Supernovae. *The Astrophysical Journal*, 710(2):1654, 2010.
- [6] A. Bartenev and B. Gelfand. Spontaneous initiation of detonations. *Progress in Energy and Combustion Science*, 26(1):29–55, 2000.
- [7] J. B. Bell, M. S. Day, C. A. Rendleman, S. E. Woosley, and M. Zingale. Direct Numerical Simulations of Type Ia Supernovae Flames. II. The Rayleigh-Taylor Instability. *The Astrophysical Journal*, 608(2):883, 2004.
- [8] E. Brooker, T. Plewa, and D. Fenn. SN Ia DDT Explosions Powered by the Zel’dovich Reactivity Gradient Mechanism. In *American Astronomical Society Meeting Abstracts*, volume 53 of *American Astronomical Society Meeting Abstracts*, page 509.07, 2021.
- [9] D. S. Burgess and M. G. Zabetakis. Detonation of a flammable cloud following a propane pipeline break: the December 9, 1970, explosion in Port Hudson, Mo. 1973. <https://www.osti.gov/biblio/7351990>.
- [10] Ciaraldi-Schoolmann, F., Seitzzahl, I. R., and Röpke, F. K. A subgrid-scale model for deflagration-to-detonation transitions in type ia supernova explosion simulations - numerical implementation. *Astronomy and Astrophysics*, 559:A117, 2013.
- [11] A. Cohen, S. M. Kaber, S. Müller, and M. Postel. Fully adaptive multiresolution finite volume schemes for conservation laws. *Mathematics of Computation*, 72:183–225, 2003.
- [12] P. Colella and P. R. Woodward. The Piecewise Parabolic Method (PPM) for gas-dynamical simulations. *Journal of Computational Physics*, 54(1):174 – 201, 1984.
- [13] R. Courant, K. Friedrichs, and H. Lewy. On the Partial Difference Equations of Mathematical Physics. *IBM Journal of Research and Development*, 11(2):215–234, 1967.

- [14] W. Doering. Ueber den detonationsvorgang in gasen. *Annalen der Physik*, 435(6-7):421–436, 1943.
- [15] C. Federrath, J. Roman-Duval, R. S. Klessen, W. Schmidt, and M. M. Mac Low. Comparing the statistics of interstellar turbulence in simulations and observations. Solenoidal versus compressive turbulence forcing. *Astronomy and Astrophysics*, 512:A81, 2010.
- [16] D. Fenn and T. Plewa. Detonability of white dwarf plasma: turbulence models at low densities. *Monthly Notices of the Royal Astronomical Society*, 468(2):1361–1372, 2017.
- [17] B. Fryxell, K. Olson, P. Ricker, F. X. Timmes, M. Zingale, D. Q. Lamb, P. MacNeice, R. Rosner, J. W. Truran, and H. Tufo. FLASH: An adaptive mesh hydrodynamics code for modeling astrophysical thermonuclear flashes. *The Astrophysical Journal Supplement Series*, 131(1):273–334, 2000.
- [18] I. Goodfellow, Y. Bengio, and A. Courville. *Deep Learning*. MIT Press, 2016. <http://www.deeplearningbook.org>.
- [19] X. Gu, D. Emerson, and D. Bradley. Modes of reaction front propagation from hot spots. *Combustion and Flame*, 133(1):63–74, 2003.
- [20] B. Gusto and T. Plewa. A hybrid adaptive multiresolution approach for the efficient simulation of reactive flows. *Computer Physics Communications*, 274:108300, 2022.
- [21] A. Harten. Adaptive Multiresolution Schemes for Shock Computations. *Journal of Computational Physics*, 115(2):319 – 338, 1994.
- [22] C. Hayashi, R. Hōshi, and D. Sugimoto. Evolution of the Stars. *Progress of Theoretical Physics Supplement*, 22:1–183, 1962.
- [23] E. P. Hicks. Rayleigh–taylor unstable flames—fast or faster? *Astrophysical Journal*, 803(2), 2015.
- [24] P. A. Höflich, A. M. Khokhlov, and J. C. Wheeler. Delayed detonation models for normal and subluminescent type Ia supernovae: Absolute brightness, light curves, and molecule formation. *The Astrophysical Journal*, 444:831, 1995.
- [25] E. Jouguet. Sur la propagation des reactions chimiques dans les gaz. *J. Math. Pures Appl.*, 1:347–425, 1905.
- [26] A. Khokhlov. Delayed detonation model for type Ia supernovae. *Astronomy and Astrophysics*, 245:114–128, 1991.
- [27] A. M. Khokhlov. Mechanisms for the initiation of detonations in the degenerate matter of supernovae. *Astronomy and Astrophysics*, 246(2):383–396, 1991.

- [28] A. M. Khokhlov, E. S. Oran, and J. C. Wheeler. Deflagration-to-detonation transition in thermonuclear supernovae. *The Astrophysical Journal*, 478(2):678, 1997.
- [29] D. P. Kingma and J. Ba. Adam: A method for stochastic optimization. In Y. Bengio and Y. LeCun, editors, *3rd International Conference on Learning Representations, ICLR 2015, San Diego, CA, USA, May 7-9, 2015, Conference Track Proceedings*, 2015.
- [30] R. Klein. Models and criteria for prediction of Deflagration-to-Detonation Transition (DDT) in hydrogen-air-steam systems under severe accident conditions Final report, 1999. http://inis.iaea.org/search/search.aspx?orig_q=RN:32014118.
- [31] A. N. Kolmogorov. The local structure of turbulence in incompressible viscous fluid for very large reynolds numbers. *Proceedings: Mathematical and Physical Sciences*, 434(1890):9–13, 1991.
- [32] K. Kuo. *Principles of Combustion*. Wiley, 2005.
- [33] J. Lee, R. Knystautas, and N. Yoshikawa. Photochemical initiation of gaseous detonations. *Acta Astronautica*, 5(11):971–982, 1978.
- [34] M. Lesieur and O. Metais. New trends in large-eddy simulations of turbulence. *Annual Review of Fluid Mechanics*, 28(1):45–82, 1996.
- [35] A. M. Lisewski, W. Hillebrandt, and S. E. Woosley. Constraints on the Delayed Transition to Detonation in Type IA Supernovae. *The Astrophysical Journal*, 538(2):831–836, 2000.
- [36] S. MacNamara and G. Strang. *Operator Splitting*, pages 95–114. Springer International Publishing, Cham, 2016.
- [37] P. MacNeice, K. M. Olson, C. Mobarrry, R. de Fainchtein, and C. Packer. Paramesh: A parallel adaptive mesh refinement community toolkit. *Computer Physics Communications*, 126(3):330–354, 2000.
- [38] F. Mattioli, C. Porcaro, and G. Baldassarre. A 1D CNN for high accuracy classification and transfer learning in motor imagery EEG-based brain-computer interface. *Journal of Neural Engineering*, 18(6):066053, 2021.
- [39] J. C. Niemeyer and S. E. Woosley. The Thermonuclear Explosion of Chandrasekhar Mass White Dwarfs. *The Astrophysical Journal*, 475(2):740–753, 1997.
- [40] J. C. Nienmeyer, W. Hillebrandt, and S. E. Woosley. Off-center deflagrations in chandrasekhar mass type ia supernova models. *The Astrophysical Journal*, 471(2):903, 1996.
- [41] K. Nomoto, D. Sugimoto, and S. Neo. Carbon Deflagration Supernova, an Alternative to Carbon Detonation. *Astrophysics and Space Science*, 39:L37, 1976.

- [42] K. Nomoto, F. K. Thielemann, and J. C. Wheeler. Explosive nucleosynthesis and Type I supernovae. *The Astrophysical Journal Letters*, 279:L23–L26, 1984.
- [43] A. Nonaka, A. J. Aspden, M. Zingale, A. S. Almgren, J. B. Bell, and S. E. Woosley. HIGH-RESOLUTION SIMULATIONS OF CONVECTION PRECEDING IGNITION IN TYPE Ia SUPERNOVAE USING ADAPTIVE MESH REFINEMENT. *The Astrophysical Journal*, 745(1):73, 2012.
- [44] T. O’Malley, E. Bursztein, J. Long, F. Chollet, H. Jin, L. Invernizzi, et al. Kerastuner. <https://github.com/keras-team/keras-tuner>, 2019.
- [45] E. S. Oran and V. N. Gamezo. Origins of the deflagration-to-detonation transition in gas-phase combustion. *Combustion and Flame*, 148(1):4–47, 2007.
- [46] D. L. C. B. (Oxon.). Vi. on the rate of explosion in gases. *The London, Edinburgh, and Dublin Philosophical Magazine and Journal of Science*, 47(284):90–104, 1899.
- [47] H. J. Pasman, C. Fouchier, S. Park, N. Quddus, and D. Laboureur. Beirut ammonium nitrate explosion: Are not we really learning anything? *Process Safety Progress*, 39(4):e12203, 2020.
- [48] N. Peters. Laminar flamelet concepts in turbulent combustion. *Symposium (International) on Combustion*, 21(1):1231–1250, 1988.
- [49] N. Peters. *Turbulent Combustion*. Cambridge Monographs on Mechanics. Cambridge University Press, 2000.
- [50] T. Plewa, A. C. Calder, and D. Q. Lamb. Type ia supernova explosion: Gravitationally confined detonation. *The Astrophysical Journal*, 612(1):L37, 2004.
- [51] G. Roy, S. Frolov, A. Borisov, and D. Netzer. Pulse detonation propulsion: challenges, current status, and future perspective. *Progress in Energy and Combustion Science*, 30(6):545–672, 2004.
- [52] I. R. Seitenzahl, C. A. Meakin, D. M. Townsley, D. Q. Lamb, and J. W. Truran. Spontaneous initiation of detonations in white dwarf environments: Determination of critical sizes. *The Astrophysical Journal*, 696(1):515, 2009.
- [53] B. Settles. *Active Learning*. Synthesis Lectures on Artificial Intelligence and Machine Learning. Morgan & Claypool Publishers, 2012.
- [54] J. E. Shepherd and J. H. S. Lee. *On The Transition from Deflagration to Detonation*, pages 439–487. Springer New York, New York, NY, 1992.
- [55] H. Shima. *Functional Analysis for Physics and Engineering: An Introduction*. CRC Press, 1 edition, 2015.

- [56] J. Snoek, H. Larochelle, and R. P. Adams. Practical bayesian optimization of machine learning algorithms. In F. Pereira, C. Burges, L. Bottou, and K. Weinberger, editors, *Advances in Neural Information Processing Systems*, volume 25. Curran Associates, Inc., 2012.
- [57] R. A. Sunyaev, editor. *27. On the Theory of Detonation Propagation in Gaseous Systems*, pages 411–451. Princeton University Press, Princeton, 1992.
- [58] F. X. Timmes and F. D. Swesty. The accuracy, consistency, and speed of an electron-positron equation of state based on table interpolation of the helmholtz free energy. *The Astrophysical Journal Supplement Series*, 126(2):501–516, 2000.
- [59] P. A. Urtiew, A. K. Oppenheim, and S. O. Saunders. Experimental observations of the transition to detonation in an explosive gas. *Proceedings of the Royal Society of London. Series A. Mathematical and Physical Sciences*, 295(1440):13–28, 1966.
- [60] J. Von Neumann. Progress report on the theory of shock waves. *National Defense Research Committee, Division*, 8, 1943.
- [61] Y. Zeldovich. Regime classification of an exothermic reaction with nonuniform initial conditions. *Combustion and Flame*, 39(2):211–214, 1980.
- [62] Y. B. Zel’dovich, V. B. Librovich, G. M. Makhviladze, and G. I. Sivashinskii. On the onset of detonation in a nonuniformly heated gas. *Journal of Applied Mechanics and Technical Physics*, 11(2):264–270, 1970.
- [63] M. Zingale, A. S. Almgren, J. B. Bell, A. Nonaka, and S. E. Woosley. Low mach number modeling of type ia supernovae. iv. white dwarf convection. *The Astrophysical Journal*, 704(1):196, 2009.

BIOGRAPHICAL SKETCH

Brandon Gusto began his undergraduate studies at Florida State University in 2013, majoring in mechanical engineering. He completed his Bachelor of Science degree in the Spring of 2017 with a double major in mechanical engineering and applied mathematics. He decided to stay at Florida State to continue his studies as a PhD student in the Department of Scientific Computing after meeting with professors and discussing research plans. While in the department Brandon studied finite volume schemes and wavelet-based adaptive mesh refinement in application to astrophysics problems under the supervision of his advisor, Dr. Plewa. In 2020 he was awarded the SMART scholarship from the Department of Defense. Upon successfully defending his dissertation, Brandon is expected to join the Naval Undersea Warfare Center Division Newport in Newport, Rhode Island as a civilian research scientist.